Method development for PILS-IC for large volume environmental chamber experiments on amine-based aerosol

Donald Cameron, BSc

Department of Chemistry and Biomolecular Sciences

Macquarie University

October 2014

Contents

Abstract III

Statement by the Candidate IV

Acknowledgements V

List of Abbreviations VII

Chapter 1. Introduction 1

- 1.1 Aerosol – Definition and description 1
- 1.2 The significance of Aerosols 2
- 1.3 Aerosol source and composition 4
- 1.4 Organic Aerosol 5
- 1.5 Global SOA emissions 7
- 1.6 Aerosol nucleation 8
- 1.7 Amines and SOA 9
- 1.8 Gas-phase chemistry of SOA formation 11
- 1.9 Common analysis and characterisation methods 17
- 1.10 Summary 19
- 1.11 Project Aims 20

Chapter 2. Chamber description and characterisation 21

- 2.1 Description of CSIRO smog chamber 21
- 2.2 Gas sample injection system 21
- 2.3 Liquid sample injection system 23
- 2.4 Monitoring Instruments 24
- 2.5 Chamber characterisation 25
  - 2.5.1 Propene/NO_x experiments 26
  - 2.5.2 NO_2 photolysis rates 28
  - 2.5.3 Wall loss of O_3 29
  - 2.5.4 Particle wall loss 30
  - 2.5.5 Outstanding characterisations 34
- 2.6 Further chamber improvements 34

Chapter 3. Particle-into-Liquid sampler and Ion Chromatography 35

- 3.1 Particle-into-Liquid Sampler 35
- 3.2 Ion chromatography 36
- 3.3 Calibration experiments 36

- 3.3.1 Cations 37
- 3.3.2 Anions 41
- 3.4 Contamination experiment 43
- 3.5 Internal Standard 45
  - 3.5.1 Make-up 46
  - 3.5.2 Flow rate into PILS 48
- 3.6 MEA limit of detection (LOD) 48

Chapter 4. MEA chamber experiments 50
- 4.1 MEA test injections 50
- 4.2 MEA photooxidation experiment 51

Chapter 5. Conclusions and Outlook 55

References 56

Appendix I 60

Abstract

Fugitive emissions of amines, such as monoethanolamine (MEA, 2-aminoethan-1-ol) or piperazine (PZ, diazacyclohexane) from industrial plants have the potential to generate aerosol under photooxidative conditions, yet the reaction mechanisms and nucleation process of these amine-systems are poorly understood.

This project aimed at developing a methodology to analyse the nucleation process(es) of these amine emission. This included characterising CSIRO's new third generation environmental chamber and incorporating a semi-online Particle-Into-Liquid Sampler/Ion Chromatography (PILS-IC) system. The PILS-IC is required for the direct identification and quantification of water-soluble organic and inorganic fractions of aerosol mass.

Chamber characterisation was achieved through several experiments including the determination of the NO_2 photolysis rate (0.512 ± 0.027 s^{-1}), the wall loss rate of ozone $(5.6112 \pm 0.0011) \times 10^{-7}$ s^{-1} and the wall loss coefficient β for particles in the bins 54.1 – 181.1 nm. During MEA irradiation experiments, the PILC-IC showed some expected trends. However, there are still several chamber auxiliary mechanisms and instrument refinements which require attention before the next stage.

We anticipate that by incorporating the proposed changes described in the work, future experiments will allow the generation of data enabling the examination and the proposition of the nucleation process(es) of amine-aerosol.

Statement by the Candidate

I, Donald Cameron, state that the work presented within this thesis was not submitted as part of a higher degree at any University or institution other than Macquarie University. I have indicated the source of any information that is not my own, that has been used throughout this thesis. The work of others utilised during this work has been acknowledged within this text. No ethics approval was required for this work.

....
Donald Cameron Date

Acknowledgements

The completion of this project was not possible without the contribution of several individuals. I would like to express my gratitude for their support during my Masters of Research thesis.

First, I would like to thank my supervisor Dr. Ian Jamie for his support and guidance throughout the project. Your calm attitude reduced the worries of not obtaining enough data during this short time, for that I am very thankful.

Secondly, many thanks to Dr. Dennys Angove, who was my associate supervisor at the CSIRO and made me very welcome in his team. Thank you for giving me the opportunity to learn operating the chamber, but also to network in the aerosol community

Thirdly, to Dr. Stephen White. Without you, many things would not have been completed during this project. Not only did you assist me on getting my know-how on chamber operations up to speed, but you contributed significantly in obtaining and understanding the generated data by performing the experiments together, discussions and proof checking my numbers. Thanks for all your contributions mate.

Also, I would like to express special thanks to these three, as not only did they support my academic career, but also actively encouraged me to pursue my dreams in my swimming career. Thank you for the understanding and the willingness to compromise, without your support, I would not have been able to perform to the level I did and make the Swiss National Team.

Next, to all the people who made life in the offices fun and bearable, such as the emissions people and Chris from IM&T at CSIRO, and the people in room 204, Jason, Soo, Erin, Asha, Ping, Kalpa, Nic and Teresa. Most importantly though, thanks to all of my good friends Tom, Roshana, Ryan, Harry, Raha, Ben, Yvonne, Dave and Dave, and the others from our masters cohort. Your friendship and the fun lunch breaks we have is the reason I still love going to university.

To Dr. Chris McRae, who helped me continue my project by lending me some chemicals, bridging the time it required for my orders to come in.

To my coach Greg. Thank you for getting me to where I am in my swimming career, but also for the support outside of the pool. Your attitude has allowed me to find the perfect balance between sport and academia.

On that note, many thanks to the people involved in supporting high performance sport at Macquarie University. The infrastructure you have provided has allowed me to excel both in sports and academia.

Many thanks to my former house mates Kate and Adam, thanks for helping out whenever you could.

I’d also like to express my gratitude to Caroline Moir, for being my linguist side-kick and helping me proof-read my work.

I am extremely grateful to the Hannan family, who provided me with a very welcoming temporary home, when I unexpectedly had to move out from my shared housing arrangement and hence deferred the stress of finding a new home until after I finished my thesis, you guys are a life saver!

Lastly but most importantly, to all my family back home in Switzerland. Thank you Mam and Dad for your continued love and support, enabling me to stay, live, study and train in Australia. Thank you to my sisters Sheena and Fiona, who keep looking out for me even though I’m on the other side of the globe. Without you all, the past six years would not have been possible.

List of Abbreviations

Ac: Acetate

AMP: 2-Amino-2-methyl-1-propanol

AMS: Aerosol Mass Spectrometer

AVOC: Anthropogenic Volatile Organic Compound

b.p: boiling point

BLB: Blacklight Blue

BTEX: benzene, toluene, ethylbenzene and xylene compounds

BVOC: Biogenic Volatile Organic Compound

CCS: Carbon Capture and Storage

CCN: Cloud Condensation Nuclei

CPC: Condensation Particle Counter

CSIRO: Commonwealth Scientific and Industrial Research Organisation

DEA: diethanolamine

EC: Elemental Carbon

EI: Electron Impact

ESI: Electrospray Ionisation

FID: Flame Ionisation Detection

FTIR: Fourier Transform Infrared Spectroscopy

GC/MS: Gas Chromatography – Mass Spectrometry

Gly: Glycolate

IC: Ion Chromatography

IN: Ice Nuclei

IPCC: The International Panel for Climate Change

IR: Infra-Red

IRMS: Isotope Ratio Mass Spectrometry

LC/MS: Liquid Chromatography – Mass Spectrometry

LOD: Limit of Detection

LOQ: Limit of Quantification

MDEA: methyldiethanolamine

MEA: monoethanolamine

MFC: Mass Flow Controller

NMR: Nuclear Magnetic Resonance

NO_x: Nitric Oxide + Nitrogen Dioxide

OA: Organic Aerosol

OC: Organic Carbon

OPM: Organic Particulate Matter

Ox: Oxalate

PAN: Peroxyacylnitrates

PILS: Particle-into-Liquid Sampler

PM: Particulate Matter

POA: Primary Organic Aerosol

ppbv: parts per billion by volume

ppmv: parts per million by volume

PZ: piperazine

RF: Radiative Forcing

RH: relative humidity

RT: Room Temperature

RO: Alkoxy radical

RO_2: Peroxy Radical

SMPS: Scanning Mobility Particle Sizer

SOA: Secondary Organic Aerosol

SVOC: Semi-Volatile Organic Compound

TC: Total Carbon

TEA: triethanolamine

TOC: Total Organic Carbon

UV: Ultraviolet Light

UFBL: unfiltered blacklight

VOC: Volatile Organic Compound

Chapter 1. Introduction

Aerosol is suspended particulate matter in the atmosphere and arises from natural and anthropogenic sources, such as sea spray, volcanoes and combustion [1]. Its composition and concentration depends on its source and local sources and sinks, such as reactions with oxidative agents that include ozone, hydroxide radical and nitrate radical [1-3]. Aerosol is of great interest as it has local and global impacts. On a local scale, decreased air quality leading to adverse health effects on humans, such as cardiovascular and respiratory illnesses are of concern [2, 4]. On a global scale aerosol has an impact by altering the Earth's energy balance and influencing cloud cover and longevity [3, 5, 6].

Secondary organic aerosol (SOA) contributes 35-73 % to the total aerosol mass [7]. SOA is produced by gas-to-particle conversion reactions from (semi-) volatile compounds in the atmosphere. The reaction mechanisms are complex and poorly elucidated [8]. Therefore, improving the understanding of aerosol nucleation and growth processes remains of importance, and will lead to better models of atmospheric processes [9-11].

Recently attention has been given to aliphatic amines, which are emitted from agriculture, industry and carbon capture and storage (CCS) technology [12, 13], as their transformation pathways and aerosol formation potentials are not well understood [12]. Some studies have suggested that they can promote aerosol nucleation [14, 15].

In order to analyse aerosol, a range of analytical techniques have to be employed to achieve a satisfactory analysis. Angove *et al.* [16] have shown that research on amine based aerosol is not without its challenges. As a consequence, standard environmental chamber experimental procedures need to be re-evaluated and new analytical tools are required for elucidating the nucleation behaviour of amine volatile organic compounds (VOCs). This thesis will focus on the development of methodologies to analyse amine-based aerosol in chamber experiments.

1.1 Aerosol – Definition and description

Aerosol is defined as a collection of fine particles that can be solid, liquid or both, suspended in a gas [1]. It can be categorised into dust, fog, fume, haze, mist, smog, smoke and soot depending on the particle diameter, which ranges between a few nanometres up to tens of micrometres, as well as its origin. Aerosol may consist of inorganic and organic matter, emitted either directly into the atmosphere from natural or anthropogenic sources (primary aerosols) or formed as a result of chemical transformation of atmospheric gases (secondary aerosols) [1].

Aerosol can be divided into three particle classes, based on particle size: ultrafine, fine and course. Ultrafine particles are primarily formed in the *nuclei mode* by nucleation and condensation of combustion products and have a diameter of ≤0.1 µm. In the atmosphere these particles are low in abundance, as they are incorporated into larger particles through coagulation or aggregation. Fine particles reside in the *accumulation mode*, have a diameter of 0.1 to 2.5 µm and are formed by particle coagulation of *nuclei mode* particles and vapour condensation. Fine particles contribute to the majority of the aerosol, as particle removal in this mode is highly inefficient. Coarse particles have a diameter larger than 2.5 µm, are typically formed by mechanical processes, such as sea spray or dust carried by wind and are the major contributor to aerosol mass [1].

Aerosol can be removed from the atmosphere either by wet or dry deposition. Dry deposition is governed by convective transport, diffusion and surface deposition. However, the dominant mode of aerosol removal is wet deposition. As aerosol particles can act as cloud condensation nuclei (CCN) or ice nuclei (IN), water condensing on the CCN/IN scavenges and washes out the CCN/IN and other aerosols from the atmosphere with rain, fog or snow [3]. While all particle sizes are prone to wet and dry deposition, due to their size, coarse particles are typically removed quickest from the atmosphere by settling out and/or deposition [1].

1.2 The significance of Aerosols

It has become increasingly evident that aerosol has local, regional and global affects through highly uncertain and complex interactions with the atmosphere and the environment. Therefore understanding aerosol formation, its chemical transformations, its sinks, its composition and its impacts is vital [8, 17, 18].

Aerosol has a global effect by altering the radiative forcing of the Earth through direct light scattering, absorption and through cloud formation. The International Panel for Climate Change (IPCC) defines radiative forcing (RF) as the net change to the Earth's energy balance caused by an external force [6], where warming effects on the climate system are called positive RF, whereas cooling effects is negative RF (see **Figure 1.1**). Aerosol influences RF either by aerosol-radiation interactions (ari; also known as direct RF) or aerosol-cloud interactions (aci; also known as indirect RF).

For direct RF, the particulate matter alters the RF by either absorbing or scattering incoming radiation [19]. The overall effect on the RF depends on the relative humidity, incoming wavelength, atmospheric loading and the distribution of aerosol in the horizontal and vertical in a given location [6]. While scattering-inducing aerosols have a negative RF, absorbing particles lead to a positive RF.

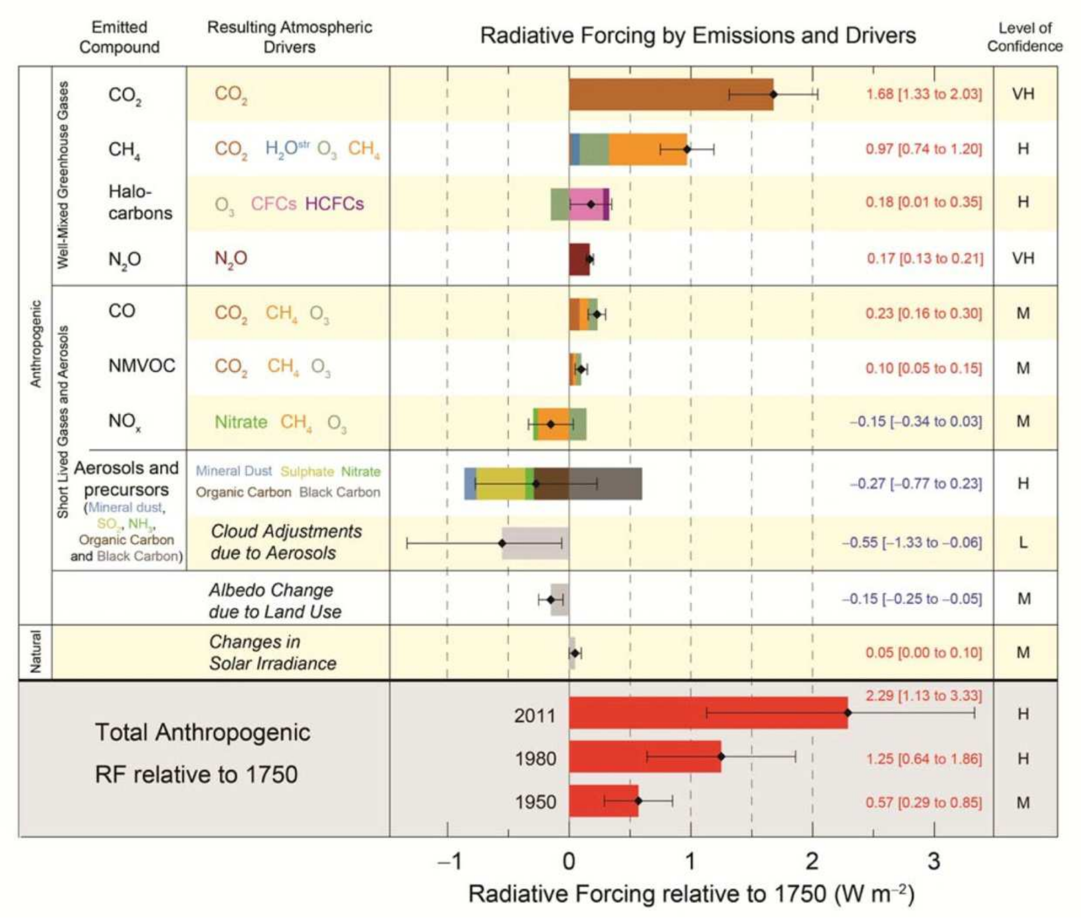

Figure 1.1: Summary of major contributors to changes in radiative forcing relative to 1750 [6].

Aerosol has an indirect global effect by influencing cloud cover and life time, as it can act as CCN or IN [3, 20]. When the relative humidity (RH) reaches water vapour supersaturation (RH > 100%), water molecules will be either adsorbed to or absorbed by the aerosol particles, as long as the RH has reached the CCN's or IN's specific critical supersaturation point [3]**.** The critical supersaturation is dependent on the particles diameters and composition. Therefore an increase in CCN and IN will alter the contributions to the climate system by the Twomey, the Albrecht, thermodynamic and glaciation effects. This in turn changes the local and global radiative energy and hydrological balance [3]**.** The Twomey effect describes the change in reflection of solar radiation by increasing the amount of small cloud particles, while the Albrecht effect describes the prolongation of cloud life, as smaller cloud particles are less likely to coagulate and precipitate [3, 20]. The thermodynamic effect describes the delay of freezing, while the glaciation effect describes an increase of precipitation efficiency with an increase of IN [3].

Due to the complex interaction between direct RF and changes to cloud formation and longevity patterns, it is still not clear whether increasing the aerosol load in the atmosphere leads to a positive feedback loop (enhance global warming) or a negative feedback loop (cooling effect) [3].

On a local scale, the most obvious effect of increased levels of aerosol mass is a decrease in visibility. In areas with high vegetation, such as in the Blue Mountains in the West of Sydney, Australia, it is not uncommon to observe a blue haze [17], while in heavily polluted urban areas smog will have an even more profound effect on visibility [9, 21].

Adverse effects to human health remain the major source of concern for particulate matter. Ultrafine particles are of great concern, as they are sufficiently small to pass through membranes of the respiratory tract and enter the blood stream or even be transported along olfactory nerves into the brain [22, 23].

As the health, radiative and hygroscopic effects of particulate matter are highly dependent on its size and structure, it remains an important requirement to analyse the particles physical and chemical properties.

1.3 Aerosol source and composition

Aerosol originates from a range of sources and is classified into either primary aerosol, which is emitted directly into the atmosphere by mechanisms such as the uplift of sea salt or dust by wind, or secondary aerosol, which is the result of chemical gas-phase reactions yielding particulate matter [1, 2, 18]. Aerosol may consist of varying proportions of inorganic, organic and biological material. Typically, salts and mineral dust particles are classified as inorganic, whereas organic compounds and black carbon are organic and spores and pollen are biological aerosols [3, 9]. **Table 1.1** lists and categorises aerosol according to size and source

Table 1.1: Major sources and composition of aerosol [1]

Size range	**Type**	**Primary source**	**Secondary source**
Fine	Sulphates	Volcanic eruptions, sea salt, gypsum	Photooxidation of biogenic gases, volcanic and anthropogenic SO_2
	Nitrate	Combustion, fertilisers	HNO_3/NH_3 and NO_x reactions
	Ammonium	Transportation sources, fertilisers	$(NH_4)_2SO_4/NH_4NO_3$
	Organic carbon	Semi- or non-volatile compounds	Photooxidation of volatile organic compounds
	Elemental carbon	Fossil fuel burning, biomass burning	-
Coarse	Nitrate	Combustion, fertilisers	Heterogeneous reactions on particle surfaces
	Minerals (Si, Ca, Mg, Al and Fe)	Crustal material (rock & soil), volcanic eruptions	-
	Biological material	Pollen, spores, plant fragments, microorganisms	-

1.4 Organic Aerosol

The organic fraction of aerosol can be the major component of the aerosol load, especially in areas with dense vegetation, such as forests, high biologically activity, such as plankton blooms or anthropogenic activity, such as urban areas [9, 24]. Conventionally the total carbon (TC) content of aerosol is defined as the sum of all carbon within the particulate matter that is not from inorganic sources. TC can be further divided into organic carbon (OC) and elemental carbon (EC). EC is usually defined as carbonaceous species which have graphite-like optical properties. Both OC and EC quantity can be determined by thermo- optical techniques, where various temperature ramps and oxidising atmospheres are employed to separate out thermal carbon fractions [25]. The total mass of organic particulate matter (OPM) is estimated by multiplying the OC mass by a factor of 1.5-2, depending on the assumed average molecular composition including the prevalence of non-carbon atoms, such as H, O, N, S etc. [3].

Primary organic aerosol (POA) consists of particles that are directly emitted into the atmosphere or semi-volatile vapours that condense at ambient atmospheric conditions. POA sources include natural and anthropogenic biomass burning, fossil fuel combustion, and wind-driven suspension of biological material and organic compounds found within sea spray [3, 9].

SOA forms as a result of chemical reactions in the atmosphere that convert volatile organic compounds (VOC) into semi-volatile gases or particulate matter. VOCs are determined to be all atmospheric organic vapour-phase species, excluding methane, CO and CO_2 [1]. Depending on the emission source, VOCs are termed either biogenic (BVOC) or anthropogenic (AVOC).

BVOCs are emitted by vegetation, soils and oceans. They may consist of terpenes, which are compounds composed of isoprene (C_5H_8) units, terpenoids, which consist of isoprene units containing oxygen in various functional groups which may have undergone (de)methylation [26]. A wide range of alkanes, alkenes, organic acids, carbonyls, alcohols, esters and ethers are additionally categorised as BVOCs, yet unlike the terpenes and terpenoids, their emissions have been poorly investigated [27]. **Figure 1.2** shows a selection of BVOCs [1, 26].

AVOCs consist of alkanes, alkenes, aromatics, oxygenated VOCs and halogenated VOCs, which arise from industrial and domestic solvent use and fuel combustion [1, 26, 28]. In urbanised areas, the predominant species of AVOCs are benzene, toluene, ethylbenzene and xylene compounds (BTEX), contributing up to 60 % to the VOCs. BTEX are not only of concern due to their carcinogenic and chronic health effects, but also due to their capability to form SOA [29-31].

Determining aerosol composition remains a challenging task, as the complex mechanism for aerosol genesis leads to a large array of particles. Slight changes in external factors can lead to the generation of new families of particles. Additionally, particles can show variable composition from core to surface. Either the particles possess a uniform internal composition with a high diversity of surface constituents, or the external layer has a more uniform composition, while the particle core consists of heterogeneous domains, which complicate the spatial analysis of aerosol [3, 9].

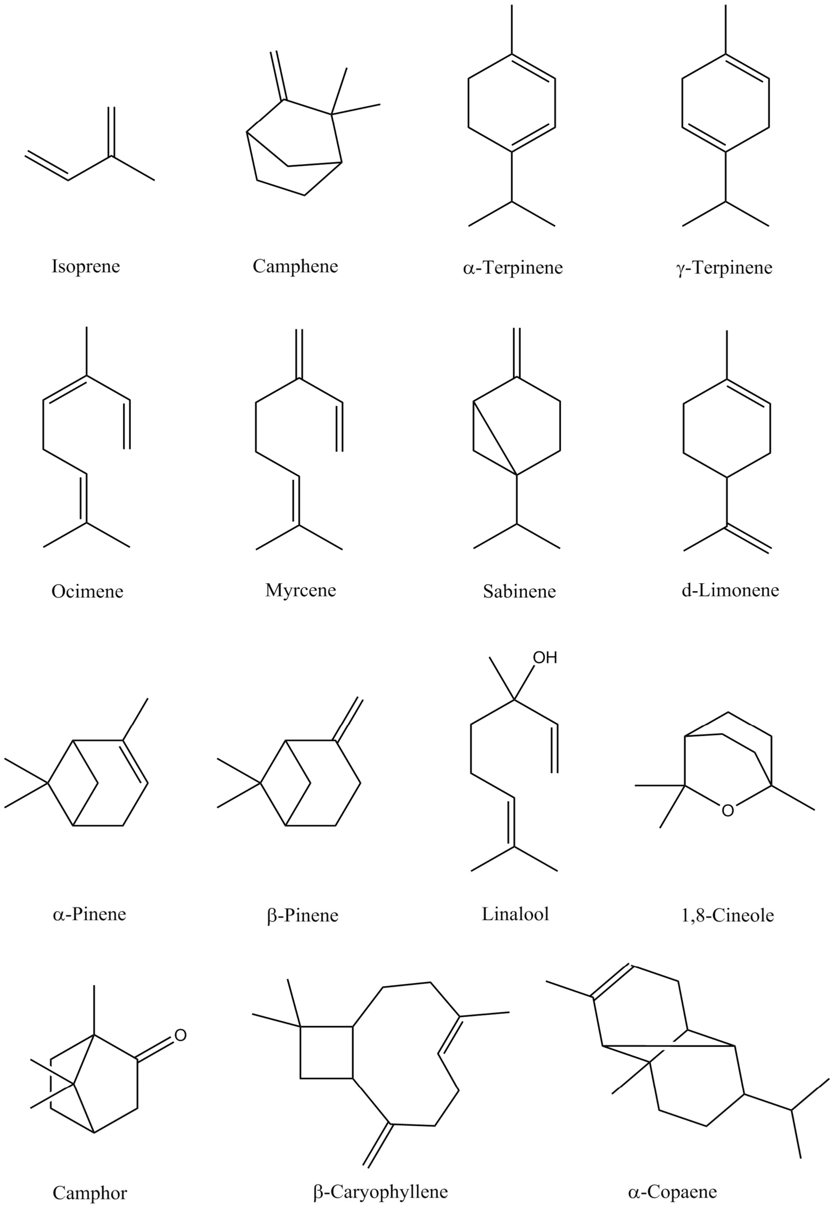
Isoprene
Camphene
α-Terpinene
γ-Terpinene
Ocimene
Myrcene
Sabinene
d-Limonene
OH
α-Pinene
β-Pinene
Linalool
O
1,8-Cineole
O
Camphor
β-Caryophyllene
α-Copaene

Figure 1.2 Structures of isoprene and selected monoterpenes, sesquiterpenes and terpenoids

1.5 Global SOA emissions

In order to estimate the global SOA emissions, two different modelling approaches are utilised. The first and most common approach is the bottom-up estimate, where the known BVOC and AVOC fluxes are pooled together with the results from chamber oxidation experiments to estimate the global organic aerosol production [18]. Chamber experiments are performed in a specifically designed closed vessel and allow researchers to simulate atmospheric conditions, reactions and processes in a highly controlled environment (volume, temperature, mixing ratios etc.), reducing the complexity of the atmosphere and allowing for comprehensible observations and results. When analysing oxidative reactions, compounds that form photooxidative species under UV-irradiation, such as NO_x and OH-radicals, are introduced before the experiment is started by exposing the gas mixture to UV-light. Using this method, a total SOA production of 12-70 Tg yr^{-1} has been estimated [32].

The second method is the top-down approach. Here the SOA production rates are inferred based on estimates of VOC fate and removal processes [17]. Within the top-down approach, the SOA production can be inferred by four different basic assumptions, each of which yields different production fluxes. Using a global mass balance for VOC emission and removal as the starting point, it has been estimated that 510-910 Tg C yr^{-1} in SOA is produced yearly, while SOA deposition and oxidation models estimate 225-575 Tg C yr^{-1}. When comparing SOA production with sulphate aerosol sources, models estimate a total SOA production of 140-540 Tg C yr^{-1} and estimates based on maintaining the global mean SOA distribution yield a flux of 223-615 Tg C yr^{-1} [17].

The top-down estimates yield significantly higher values than the bottom-up calculations. This large discrepancy may arise from the bottom-up approach heavily relying on data generated by chamber experiments, which are of shorter duration and cannot generate the final oxidative products that are found in the atmosphere. Therefore, it is plausible that the bottom-up estimates lead to underestimations of SOA production.

1.6 Aerosol nucleation

Three mechanisms which lead to SOA formation from VOCs have been identified [3, 9]:

1. Homogeneous nucleation. This is the process during which a species of semi-volatile organic compounds (SVOC) undergoes gas-phase reactions with the same species to form new particles.
2. Partitioning of gas-phase SVOCs into or onto pre-existing particles.
3. Heterogeneous or multiphase reactions of VOCs or SVOCs on the surface of aerosols or cloud particles

In the case of new particle formation with no pre-existing aerosols, there are four main hypotheses for homogeneous nucleation [10]. In industrial plumes, it is likely that particles are formed homogenously from a binary mixture consisting of water and sulphuric acid, if the latter is present. In the continental boundary layer, it is believed that homogenous nucleation occurs by ternary nucleation of typically water, sulphuric acid and ammonia. Another ternary system for particle generation is nucleation involving ammonia, nitric acid and water [1]. Field experiments and models suggest that new organic particle formation may be dominated by ternary homogenous nucleation, as the binary homogenous nucleation model can only predict nucleation rates at extreme conditions, which include low temperatures, high relative humidity, high sulphuric acid concentration and low aerosol loading [9, 33]. In the upper troposphere and lower stratosphere, it is believed that nucleation of binary, ternary or organic vapours are ion-induced [10]. Lastly, in coastal environments it is likely that homogenous nucleation involves iodide species [10, 34]. It must be pointed out that when considering these nucleation theories, the resulting particulate matter can be predominantly of inorganic nature, especially when sulphuric acid contributes significantly to the mixing ratios of the nucleating vapours. Nevertheless, these theories present a good foundation for an investigation into the nucleation mechanism of amine-based aerosol.

1.7 Amines and SOA

Amines are emitted to the atmosphere from a number of different sources, including cooking of animal flesh, biomass burning, motor vehicle exhausts, industrial processes, such as CO_2 scrubbing, and marine biota [12, 13]. Agriculture is the major source of anthropogenic ammonia emissions and mixing ratios can reach hundreds of parts per billion (ppbv) in rural areas [35]. In contrast, biogenic amines are quite common in the marine atmosphere close to high biological activity, such as at phytoplankton blooms [24, 36]. The majority of nitrogen containing aerosols of sub-micrometre size are produced by gas-to-particle reactions and it is estimated that the nitrogen containing organic aerosol species flux is 0.2-0.7 Tg yr^{-1} [37]. Despite being a small fraction of the total SOA, amines have been shown to influence particle nucleation and thus CCN formation [38], most likely due to the different reaction pathways available.

Amines are also used as co-solvents, solvents or starting materials, therefore with the growth of the chemical and pharmaceutical industry anthropogenic amine emissions have increased [39]. In recent years, carbon capture technology has been applied to new coal and natural gas power plants and in the retrofitting old ones to reduce CO_2 emissions. One form of carbon capturing technology is based on solution scrubbing, where the solutions contain aqueous monoethanolamine (MEA, 2-aminoethan-1-ol), diethanolamine (DEA, 2,2’-azanediylbis(ethan-1-ol)), triethanolamine (TEA, 2,2’,2’’-nitrilotris(ethan-1-ol)), methyldiethanolamine (MDEA, 2,2’-(methylazanediyl)bis(ethan-1-ol)) or piperazine (PZ, diazacyclohexane) [40, 41]. As the gas stream being scrubbed is in intimate contact with the solutions, these installations lead to direct or fugitive alkanoamine emission. Despite the increased application of this technology, little research has been conducted on the degradation and transformation of these alkanoamines in the atmosphere, the manner in which they initiate aerosol nucleation, or their impact on human health and environment [13].

Computer cluster modelling has revealed that amines form neutral ionic clusters with sulphuric acid ions more effectively than ammonia, and experiments have shown that they can prevent H_2SO_4 dimers from re-evaporating into the gas-phase through stabilisation effects [42, 43]. As a consequence, it is expected that amines would increase aerosol production. Recent studies have not only shown that aminium ions (R_3NH^+) can replace ammonium ions in the thermodynamically stable clusters, but also that small amines are present within these sub-3 nm clusters and enhance particle nucleation and growth [14, 15].

Early studies on chemical transformation of amines in the atmosphere concentrated on carcinogenic nitrosamines. However, the results showed rapid photolysis of the compounds of interest and therefore posed minimal health risks during daylight [44]. More recently, animal studies have shown that amine-coated ultrafine particles greatly increase the risk of thrombosis [45]. Yet, there have been few toxicological studies on aerosol generated by amines.

Consequentially, investigating the types of amine based aerosol is important. The few existing chamber or ambient air studies have concentrated on SOA production from mostly aliphatic amines, such as methylamine, dimethylamine, trimethylamine, ethylamine, diethylamine, triethylamine, which are emitted by the marine environment or animal husbandry [12, 20, 36, 38]. Results from chamber experiments [12] have shown that aliphatic amines undergo acid-base reactions with atmospheric nitric and sulphuric acid to form aminium salts. The aminium concentration is dependent on amine, acid and ammonium loading. Ammonia acts as a scavenger, as it competes with the amines for acidic compounds in the atmosphere. Amines undergo the expected photooxidative and ozonolysis processes. However, while tertiary amines tend to form non-salt aerosol, primary and secondary amines tend to only form aminium-salt derived aerosol. The major implication of the formation of non-salt vs. salt-derived aerosols is their longevity. Salt-derived aerosols were shown to be more prone to re-evaporation than the oxidised amine particulate matter [12].

In a recent report by Angove *et al.* [16], it was reported that MEA shows a different nucleation pattern than non-amine VOCs: Upon irradiation by UV lights, MEA produces aerosol immediately, while aerosol production from non-amine VOCs exhibit a delay; a phenomenon that has yet to be investigated with other amine systems.

1.8 Gas-phase chemistry of SOA formation

The formation of secondary organic aerosols usually occurs after VOCs have undergone a series of oxidative gas-phase reactions, which result in the formation of species with lower vapour pressure, leading to condensation. Even though direct photolysis by UV light and the gas-phase reactions with O_3, NO_3 and OH radicals are considered the most important VOC transformation and SOA formation pathway [8], other studies have shown that heterogeneous and particle-phase reactions cannot be neglected [9, 18].

The generation of atmospheric oxidants is shown in the **reaction schemes 1.1** to **1.8 [1]**. Ozone is formed when molecular oxygen reacts with atomic oxygen, which is turn is the product of NO_2 photolysis. A dynamic equilibrium across the **Reactions 1.1** to **1.3** is reached, as NO_2 is regenerated by ozone reacting with NO (**Reaction 1.3**) [26].

$$NO_2 + (\lambda \leq 421\text{nm}) \longrightarrow NO + O(^3P) \quad (1.1)$$

$$O(^3P) + O_2 + M \longrightarrow O_3\ (M = N_2 \text{ or } O_2) \quad (1.2)$$

$$O_3 + NO \longrightarrow NO_2 + O_2 \quad (1.3)$$

OH radicals are formed by $O(^1D)$ reacting with water. $O(^1D)$ is generated by ozone photolysis (**Reaction 1.4**) and can either be deactivated by **Reaction 1.5** to ground state $O(^3P)$ or undergo **Reaction 1.6**. Other reaction pathways that yield hydroxyl radicals are the photolysis of HONO, HNO_3, H_2O_2 and HO_2NO_2 [2].

$$O_3 + (\lambda \leq 350\text{ nm}) \longrightarrow O_2 + O(^1D) \quad (1.4)$$

$$O(^1P) + M \longrightarrow O(^3P) + M\ (M = N_2 \text{ or } O_2) \quad (1.5)$$

$$O(^1D) + H_2O \longrightarrow 2\ {}^{\bullet}OH \quad (1.6)$$

At night, the concentration of NO_3 radicals, which are formed by the reaction of NO_2 with O_3, becomes a significant for VOC transformations, as during the day these radicals have a life-time of approximately five seconds due to rapid photo dissociation into NO and molecular oxygen (**Reactions 1.8** and **1.9**).

$$NO_2 + O_3 \longrightarrow NO_3 + O_2 \quad (1.7)$$

$$NO_3 + h\nu\,(\lambda \leq 721\text{ nm}) \longrightarrow NO + O_2 \quad (1.8)$$

$$NO_3 + h\nu\,(\lambda \leq 580\text{ nm}) \longrightarrow NO_2 + O \quad (1.9)$$

Figure 1.3 illustrates a simplified schematic of VOC transformations in the troposphere. The first transformation step is either a photooxidative attack or ozonolysis, followed by a series of radical reactions with molecular oxygen, NO_x, peroxides or other radicals. In photooxidation, typically a hydrogen atom is abstracted from either a primary, secondary or tertiary carbon (**Reactions 1.10** and **1.11**), or OH or NO_3 is added across a double bond (**Reactions 1.12** and **1.13**). In ozonolysis, the ozone molecule reacts with the double bond to an ozonide before decomposing into a carbonyl and the Criegee intermediate (**Reactions 1.14)**. This intermediate either decomposes through the hydroperoxide channel to give rise to an alkyl radical, or undergoes unimolecular isomerisation (**Reaction 1.15**), or follows the stabilised Criegee intermediate channel (SCI) undergoing further reactions with water and oxidative species present in the atmosphere [8].

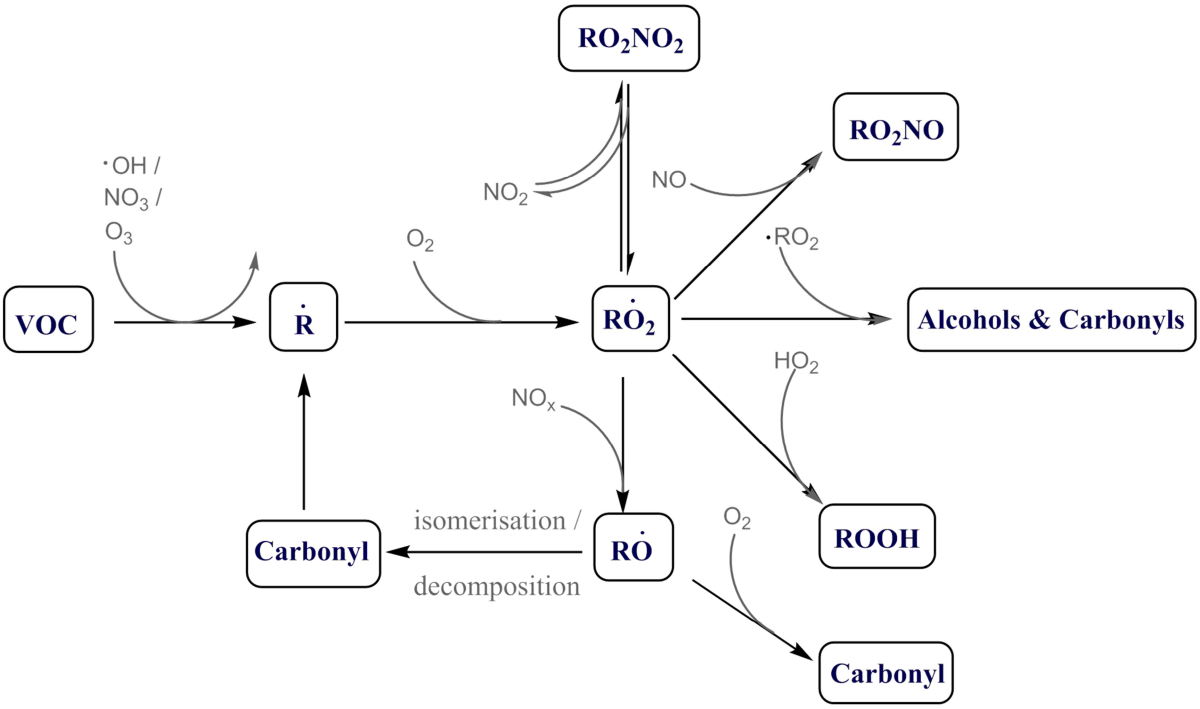

Figure 1.3 Simplified schematic for initial VOC transformation steps

The resulting radical reacts with molecular oxygen yielding organic peroxy radicals (RO_2). Peroxy radicals and the NO_x mixing ratio are crucial components for SOA production [8]. At low NO_x levels, hydroxperoxides from peroxy radical (**Reaction 1.16**) and ozonolysis reactions are a major contributor to SOA levels, whereas at high NO_x levels, RO_2 preferentially reacts with NO to form alkoxy radicals (RO) (**Reaction 1.17**) or organic nitrates (**Reaction 1.18**). Under the latter condition, peroxy radicals can also react with NO_2 to form either peroxynitrates (**Reaction 1.19**) or peroxyacylnitrates (PAN) (**Reaction 1.20**). Within the atmosphere, peroxynitrates only last for less than 1 second, whereas peroxyacylnitrates can last from hours to days, acting as a temporary reservoir for NO_x and RO_2. In the absence of NO_x, peroxy radicals can undergo cross- and self-reactions, which give rise to alkoxy radicals (**Reaction 1.21**) or organic peroxides (in the case of large RO_2 radicals) (**Reaction 1.22**), or lead to a chain terminating reaction producing carbonyls and alcohols (**Reaction 1.23**) [8].

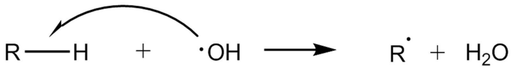

$$R{-}H + {}^{\bullet}OH \longrightarrow \dot{R} + H_2O$$

(1.10)

$$R{-}H + NO_3 \longrightarrow \dot{R} + HNO_3 \qquad (1.11)$$

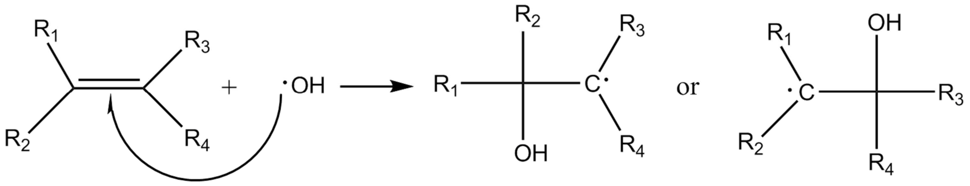
R1
R2
R3
R4
+
·OH
R1
R2
C·
R3
R4
OH
or
R1
·C
R2
OH
R3
R4

(1.12)

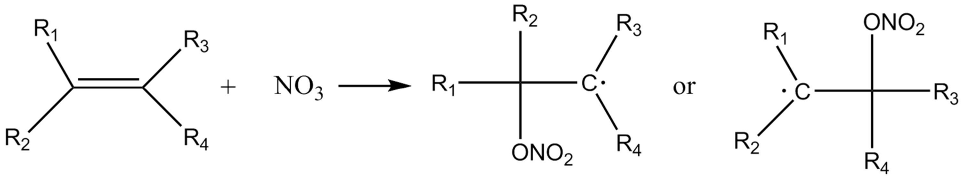
R1
R2
R3
R4
+
NO3
R1
R2
C·
R3
R4
ONO2
or
R1
·C
R2
ONO2
R3
R4

(1.13)

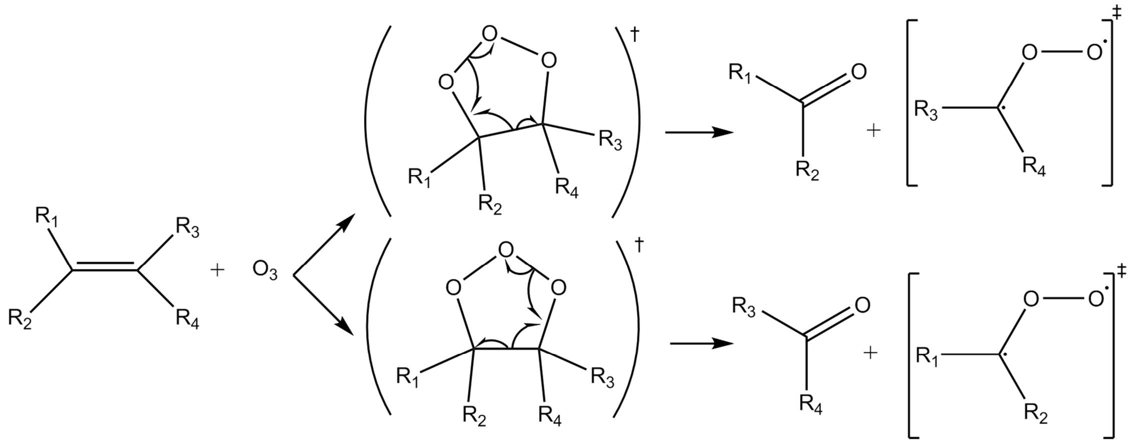
R1
R2
R3
R4
+
O3
O
O
O
R1
R2
R3
R4
†
R1
O
R2
+
O
O·
R3
R4
‡
O
O
O
R1
R2
R3
R4
†
R3
O
R4
+
O
O·
R1
R2
‡

(1.14)

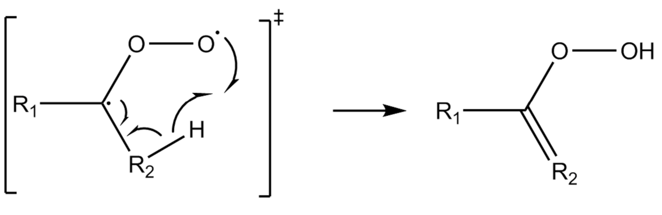
O
O·
R1
H
R2
‡
O
OH
R1
R2

(1.15)

$$R\dot{O}_2 + HO_2 \longrightarrow ROOH + O_2 \qquad (1.16)$$

$$R\dot{O}_2 + NO \longrightarrow RO + NO_2 \qquad (1.17)$$

$$R\dot{O}_2 + NO \xrightarrow{[+M]} RONO_2 \qquad (1.18)$$

$$R\dot{O}_2 + NO_2 \underset{}{\overset{[+M]}{\rightleftharpoons}} ROONO_2 \qquad (1.19)$$

$$\mathrm{RC(O)\dot{O}_2 + NO_2 \xrightarrow{+M} RC(O)OONO_2} \tag{1.20}$$

$$\mathrm{R\dot{O}_2 + R'\dot{O}_2 \longrightarrow RO^{\bullet} + R'{=}O + O_2} \tag{1.21}$$

$$\mathrm{R\dot{O}_2 + R'\dot{O}_2 \longrightarrow ROOR' + O_2} \tag{1.22}$$

$$\mathrm{RCH_2\dot{O}_2 + R'CH_2\dot{O}_2 \longrightarrow RCHO + R'CH_2OH + O_2} \tag{1.23}$$

From the data obtained from a few alkanoamine chamber experiments, Schade and Crutzen [46], Murphy *et al.* [12] and Nielsen *et al.* [47] have been able to propose transformation pathways for amines in the troposphere. **Figure 1.4** displays the photooxidative transformation pathways of amines.

The most common initial reaction step is the abstraction of a hydrogen atom either directly from the nitrogen or from one of the R-groups. The nitrogen radical can then undergo various reactions with either NO, NO_2 or oxygen to yield nitrosamines, nitramines or an imine. Products from the NO and NO_2 reactions usually yield particulate matter, which can be carcinogenic [44]. With enough water vapour present, the imine can be dissolved and converted into an aqueous amine and aldehyde and be removed by wet deposition.

If the radical was formed on one of the R-groups, reactions with oxygen can either yield an imine (only from primary and secondary amine precursors) or a peroxyl radical. The peroxyl radical can then be transformed to an alkoxy radical, which can either decompose to the nitrogen radical and an aldehyde, or react with NO_2 to yield amine nitrate, or react with oxygen to yield an amide. At low NO concentrations, self-condensation of the peroxyl radicals is an alternative pathway. Just like the imine, amides can be dissolved into an aqueous amine and acid with sufficient water vapour in the atmosphere.

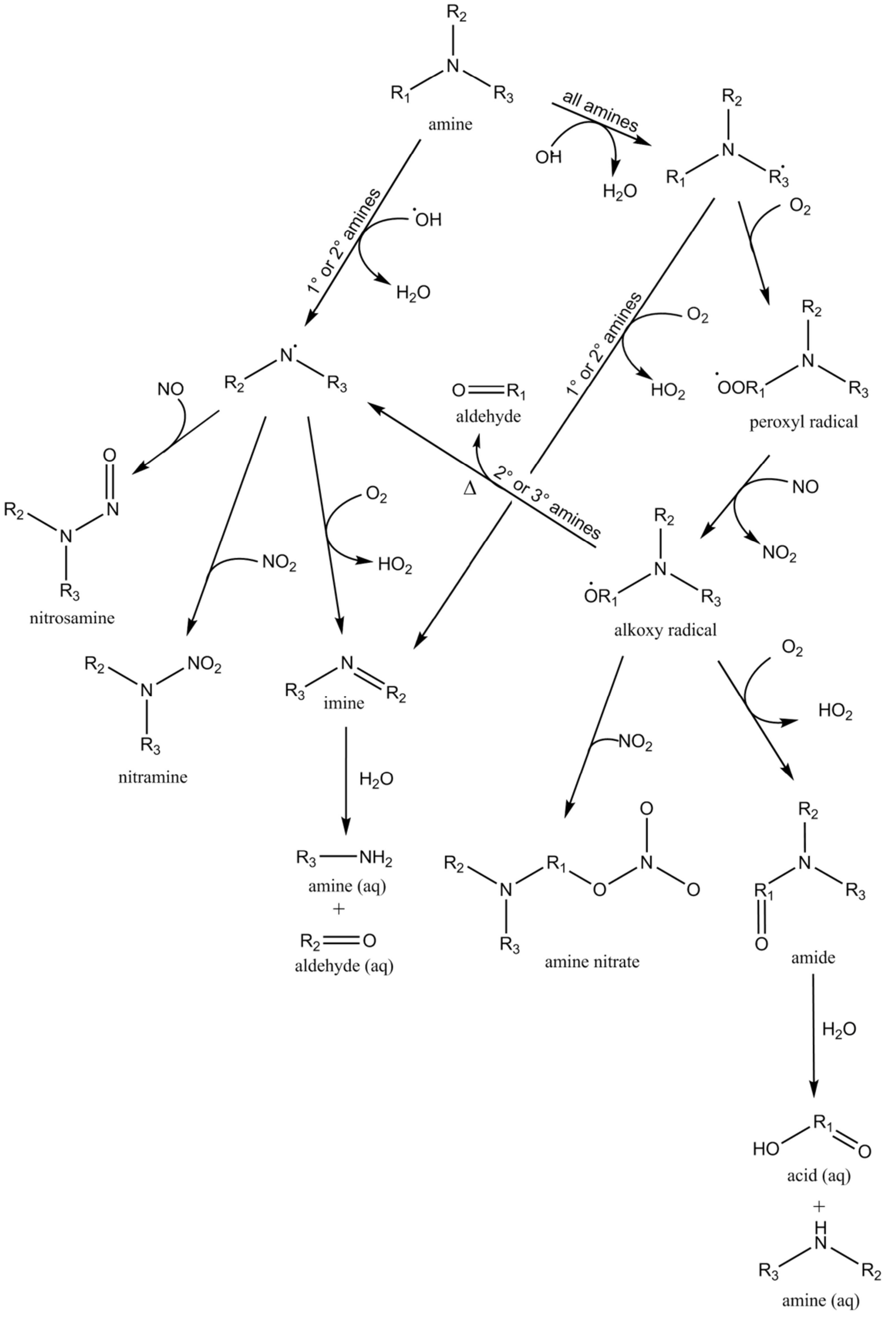
amine
all amines
OH
H_2O
1° or 2° amines
$\dot{O}H$
H_2O
O_2
1° or 2° amines
O_2
HO_2
peroxyl radical
NO
nitrosamine
aldehyde
Δ
2° or 3° amines
O_2
HO_2
NO_2
NO
NO_2
alkoxy radical
nitramine
imine
H_2O
amine (aq)
+
aldehyde (aq)
O_2
HO_2
NO_2
amine nitrate
amide
H_2O
acid (aq)
+
amine (aq)

Figure 1.4: Amine photooxidative transformation pathway in the presence of NO_x (adopted from Schade and Crutzen, Murphy *et al.* and Nielsen *et al.* [12, 46, 47]).

Figure 1.5 illustrates the potential products of alkanoamine ozonolysis. The pathway followed depends highly on the degree of saturation of the nitrogen atom. The initial step of attack by an ozone molecule yields a high energy amine oxide intermediate. It is postulated that in cases of tertiary amines, this intermediate can be stabilised to yield an alkylamine-N-oxide. However, it is more likely that this intermediate undergoes rearrangements, by shifting

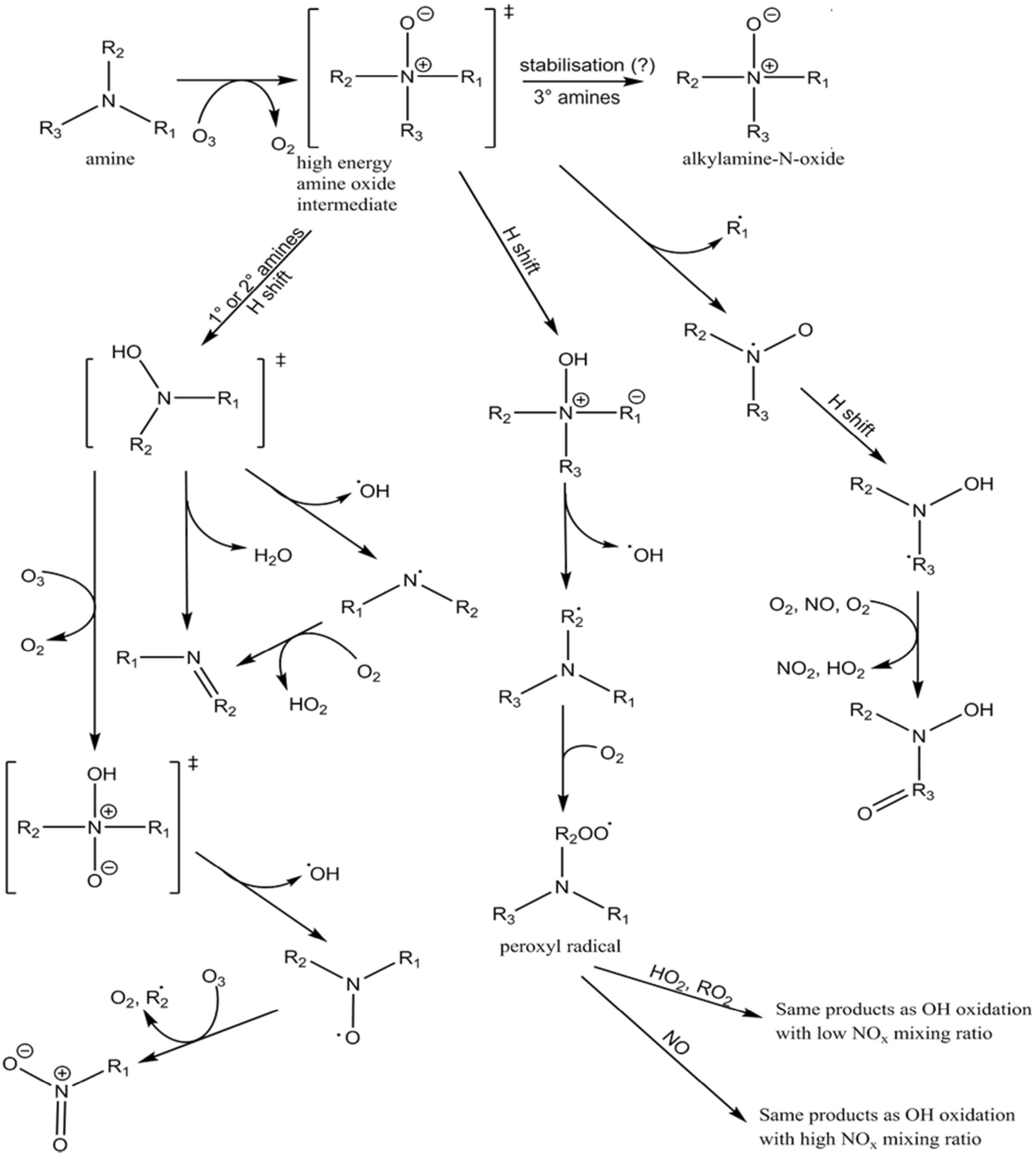
amine
O_3
O_2
high energy amine oxide intermediate
stabilisation (?)
3° amines
alkylamine-N-oxide
1° or 2° amines H shift
H shift
H shift
$\dot{R}_1$
$\cdot OH$
H_2O
O_3
O_2
O_2
HO_2
$\cdot OH$
O_2, NO, O_2
NO_2, HO_2
O_2
$\cdot OH$
O_2, $\dot{R}_2$
O_3
peroxyl radical
HO_2, RO_2
NO
Same products as OH oxidation with low NO_x mixing ratio
Same products as OH oxidation with high NO_x mixing ratio

Figure 1.5: Amine ozonolysis transformation pathway in the presence of NOx (adopted from Murphy *et al.* and Nielsen *et al.* [12, 45])

a hydrogen either from the nitrogen atom (in case of primary and secondary amines) or from one of the R-groups to the charged oxygen. Alternatively, one of the R-groups can leave as a result of radical bond breaking chemistry. In the case of primary or secondary amines, the newly formed intermediate (**Figure 1.5**) can either release a hydroxyl radical to give rise to the amine radical described in **Figure 1.4**, or form an imine through the loss of water. A further reaction pathway is for the intermediate to react with ozone. A sequential loss of a hydroxyl radical and reaction with ozone initiates an R group to break off, yielding a nitro-compound (**Figure 1.5**). When the H-shift occurs from one of the R-groups, a peroxyl radical is formed after the loss of a hydroxyl radical and the uptake of an oxygen molecule. This peroxyl radical can then undergo further transformations, which are dependent on the NO_x mixing ratios. At high NO_x mixing ratios, the radical can undergo the same transformations as shown in **Figure 1.4**. In the case of losing an R-group, which is not a hydrogen atom (**Figure 1.5**), a subsequent H-shift and reactions with two oxygen molecules and a NO molecule yields various classes of N-hydroxyl amides.

1.9 Common analysis and characterisation methods

Due to the highly complex transformation and degradation pathways, the major barrier of characterising SOA is the sheer number of individual species present in a sample. Goldstein and Galbally illustrate this issue by showing that for alkanes with 10 carbons, there are 100 possible isomers and thus more than one million C_{10} organic species if heteroatoms are included [17]. The complexity of the chemical composition has resulted in three characterisation methods: indirect, off-line and on-line techniques [18].

Indirect methods infer the SOA content by subtracting the measured POA content from the total organic aerosol content. Off-line techniques include Gas Chromatography/Mass Spectrometry (GC-MS), Gas Chromatography-Flame Ionisation Detection (GC-FID), Liquid Chromatography/MS (LC-MS), Isotope Ratio Mass Spectrometry (IRMS), optical-thermal technique for EC/OC, and Nuclear Magnetic Resonance (NMR) and Fourier Transform Infrared (FTIR) spectroscopy [18, 48-50]. FTIR can also be used for online analysis. The disadvantages of some these techniques are the collection methods and the required sample size for a qualitative analysis. In order to analyse aerosol off-line, it has to be collected (e.g. onto filters) and then extracted using methods such as solvent extraction [28], supercritical fluid extraction [51] or thermal desorption [52] prior to analysis. When using these extraction methods, typically various solvents and pre-treatments have to be employed occasionally with subsequent derivations in order to analyse the majority of the sample [18]. Despite these measures, it cannot be guaranteed that the analysed aerosol from the filters is a true representative sample of the aerosol of interest, as effects such as filter and solvent affinity may alter the true distribution of the species present. Additionally, some of these techniques provide only limited information on the chemical composition of the aerosol, such as the functional groups when using FTIR, the amount of organic carbon present in the sample when using EC/OC optical-thermal methods, or the carbon isotope ratio when using IRMS. While the latter three techniques provide information on a small class of aerosol, GC/MS and LC/MS can elucidate the individual organic compounds in the aerosol on a molecular level. However, these MS techniques are highly specific and henceforth can only analyse a very small percentage of the total aerosol mass for each individual set-up or settings.

In certain cases (semi-)on-line techniques are more favourable, especially as they do not require extraction techniques. Aerosol Mass Spectrometry (AMS) and Particle-Into-Liquid Sampler coupled to Ion Chromatography (PILS-IC) require both less time and sample quantity to produce reliable data [18]. They are however not without their limitations. The AMS instruments are commonly employed in field experiments [53, 54] and provides information on the sulphate, nitrate, ammonium, chloride and organic content of aerosol through sample fragmentation [55]. PILS-IC has been employed extensively for both field and chamber experiments [12, 18, 20]. Unlike AMS, PILS-IC does not lead to fragmentation, but separates species according to their charge [12]. However, some issues such as co-elution of species, for instance ammonium and methylammonium, and the fact that only water-soluble ionic species can be analysed remain a significant limitation of this technique.

Currently, no perfect instrument exists which provides a satisfactory analysis in terms of 100 % mass balance, chemical composition and time and size resolution. Researchers are forced to use complementary techniques to gather sufficient data to obtain an adequate analysis of aerosol mass. **Figure 1.6** is a plot of the commonly used analytical techniques applied in aerosol research.

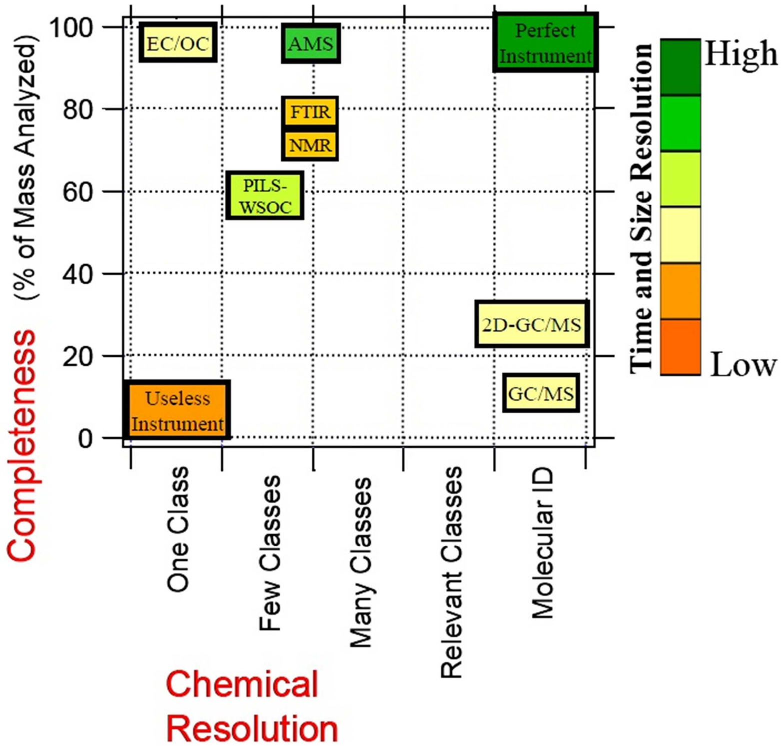

Figure 1.6: Three dimensional representation of commonly employed analytical techniques in aerosol analysis. Image adopted from Hallquist *et al.* [18].

1.10 Summary

Aerosol consists of suspended particulate matter in the atmosphere and remains of great interest due to its structural complexity, which determines its effect from a local to a global scale [1, 6]. On a global scale, aerosol not only influences RF, but is the source of CCN and IN, and therefore has the potential to change the Earth's albedo by changing cloud cover and longevity [3, 5, 6, 19, 20]. On a local scale, the most apparent consequence of high aerosol load is decreased visibility [9]. However, adverse health effects, such as a higher risk of blood clotting and pulmonary inflammation due to a prolonged exposure to high concentrations of particulate matter, are of major concern [56].

Aerosol composition depends on emission source and local atmospheric conditions. Its chemical and physical properties, such as composition, water solubility and particle shape dictate the formation, growth, chemical reactivity and removal processes of aerosol [3, 9]. One of the major sources of condensable material that eventually leads to aerosol formation is VOCs. They are either from biogenic or anthropogenic sources [1, 26, 29-31]. If the VOCs' vapour pressure is low enough, it can condense without atmospheric transformation chemistry and is considered POA. Meanwhile, particulate matter arising from VOCs that underwent photooxidative and other atmospheric reactions is considered SOA.

In recent years, carbon capture technology has received attention to reduce CO_2 emissions from industrial plants. This technology uses aqueous alkanoamines for gas scrubbing [40, 41]. As the gas stream is in intimate contact with the solvents, direct or fugitive alkanoamine emissions are inevitable. Despite the increased interest in CCS technology, little research has been conducted on the degradation and transformation of the alkanoamines in the atmosphere, how they initiate aerosol nucleation, or their impact on human health and environment by SOA formation [13].

However, currently no perfect instrument exists, which can provide a complete aerosol analysis. Therefore when analysing aerosol genesis, atmospheric transformation chemistry, and aerosol composition, researchers are forced to use complementary techniques to generate sufficient supporting data prior to attempting to elucidation and explanation of these complex mechanisms [18]. As a consequence of the current limitations, each of the three aspects on aerosols provides ample opportunities for aerosol research.

1.11 Project Aims

The long term objective of the current project is to understand nucleation process(es) for aerosol generation by the amines MEA, PZ and 2-amino-2-methyl-1-propanol (AMP). As the recent CSIRO report suggests a different nucleation behaviour for MEA in contrast to well-studied non-amine VOCs [16], the aerosol production from these species will be examined as a function of alkanoamine and NO_x loading and composition of aerosol generated will be determined in terms of organic and inorganic fractions. These data may help clear up the different nucleation behaviour.

However, before these crucial experiments can be conducted, CSIRO's new third generation environmental chamber has to be commissioned and fitted with analytical instruments tuned for the analysis of amine-based aerosol. Angove *et al.*'s work also describes the additional challenges when investigating the atmospheric chemistry of amine VOCs [16]. Therefore the immediate aim of this project is to develop a suitable methodology for analysing amines in chamber experiments by adapting or refining standard experimental procedures to this compound class. A significant proportion of this work will be dedicated to the incorporation of the new PILS-IC analytical tool, which is required to determine the water soluble organic and inorganic fractions of aerosol mass.

Chapter 2. Chamber description and characterisation

2.1 Description of CSIRO smog chamber

All experiments were performed at the CSIRO site at North Ryde in Sydney. The CSIRO indoor chamber is a rigid rectangular chamber with the dimensions of 1.98 m (height) × 5.07 m (width) × 2.46 m (breadth) giving a volume of 24.7 m^3, a surface area of 54.8 m^2 and a surface-to-volume ratio of 2.22 m^{-1}. The frame consists of light aluminium and is mounted onto an aluminium sheet, is covered by FEP 100 Teflon® film (DuPont, 0.025 mm) and enclosed by highly polished aluminium, maximising reflection. The Teflon film allows the chamber to be flexible during gas introduction and extraction, reducing variance in internal pressure and aiding mixing through wall movement.

When not in operation, the chamber is continuously flushed with clean air. The clean air is provided by a compressor unit (CompAir D22H) mounted externally to the laboratory facility and sequentially purified by a swing system consisting of charcoal and molecular sieve conditioners.

Two modules fitted with highly polished aluminium reflectors containing 40 black-lights each are mounted externally of the Teflon wall at each end of the chamber. The lights are positioned ~50 mm from the Teflon walls to minimise surface heating on the film. In each module half of the lights are filtered black-lights (Sylvania F36W Blacklight Blue, 36 W, BLB) with a primary range of 350-390/400 nm with peak intensity at 368 nm, while the other half consist of unfiltered black-lights (NEC FL40SBL lamps, 40 W, UFBL) with a primary range of 300-400 nm with some peaks between 400-600 nm and peak intensity at 365 nm. When operated simultaneously, the primary range shifts to 310-400 nm and the peak intensity to 365 nm. The Teflon walls have negligible absorption in the actinic region.

There are six transfer ports built into the chamber walls, four of which contain sample line inlets to introduce VOCs, O_3, and NO_x, and outlets to draw sampling air to the monitoring instruments. Two of the ports are used for the mirrors required for directing the FTIR's IR beam.

2.2 Gas sample injection system

Mass flow controllers (MKS Instruments, 1179B series, MFC) are used to control makeup, carrier, diluent and reactant gases injected into the chamber. There are two manifolds, one controlling carrier gases and the injection of hydrocarbons and amines (Manifold 1), while the second controls the injection of NO_x species (Manifold 2), as shown in the panel picture in

Figure 2.1. In past work it had been observed that amines formed particles prior to injection [57]. Separate manifolds are used for reactive VOC and the NO_x reagents to prevent any possibility of reaction within the manifold.

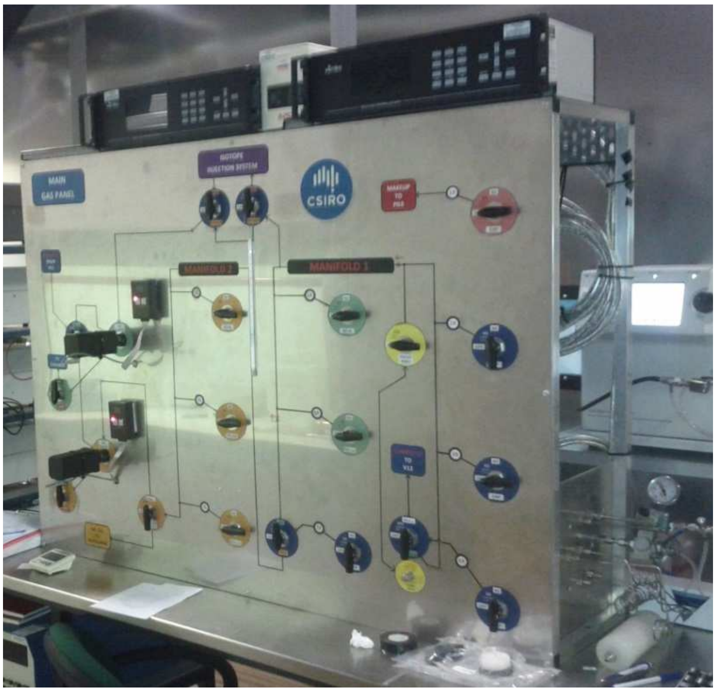

Figure 2.1: The gas control panel with digital Multi Gas Controllers (black) on top. Manifold for carrier gas and VOCs is on the right (blue and green), while the manifold for NO_x reagents is on the left (orange).

Prior to chamber operations, the mass flow controllers are calibrated by measuring the flow rates of nitrogen gas, clean air, NO in N_2, NO in He, and propene in N_2 with either a custom made bubble meter for low flow rates (5 mL min^{-1} – 200 mL min^{-1}) or a Bios Defender 510h (MesaLabs) for high flow rates (200 mL min^{-1} – 20 L min^{-1}) to determine the divergence of the flow rates at laboratory operation temperature (~23 °C) from the electronically set flows on the control panel (MKS Multi Gas Controller 647c). For each MFC, at least four different flow rates were measured in quintuplets before converting the obtained data to standard temperature (273.15 °K, T_0) and pressure (1 bar, $P°$) (STP) using the equation

$$\boldsymbol{Q_{STP} = Q_M \times \frac{P}{P^\circ} \times \frac{T_0}{T}}, \quad (1)$$

where Q_{STP} is the flow at STP, Q_M the measured flow rate (either L min^{-1} or mL min^{-1}), P is the measured pressure and T is the measured room temperature in Kelvin. For the values obtained from the bubble meter, in which process the gas stream becomes saturated in water vapour, the flows are corrected by

$$\boldsymbol{Q_{corr} = Q_M \times \frac{P - P_{H_2O}}{P}}, \quad (2)$$

where P_{H_2O} is the temperature dependant value for water vapour, which is determined using **Equation 3** [58].

$$\ln\left(\frac{P_{H_2O}}{P_c}\right) = \left(a_1\tau + a_2\tau^{1.5} + a_3\tau^3 + a_4\tau^{3.5} + a_5\tau^4 + a_6\tau^{7.5}\right) \times \frac{T_c}{T}, \tag{3}$$

where P_c is the critical water pressure (22064 kPa), T_c is the critical temperature (647.096 °K), $\tau = 1\text{-}T/T_c$, and the α-values are tabulated below in **Table 2.1**:

Table 2.1: α-values for equation 3, published by Wagner and Pruss [58].

α	1	2	3	4	5	6
value	−7.85951783	1.84408259	−11.7866497	22.6807411	−15.9618719	1.8022502

The calculated STP and RT flows for each sample point were averaged and then plotted against the electronic input values to yield calibration plots (see **Figure xI.1** in Appendix I for example). From the calibrations, propene-, NO- and NO_2-injection times, and carrier gas settings for calibrating the NO_x detector were calculated. **Equation 4** allows the calculation of chamber concentrations of the required gas for any given injection time *t*, where *Q* is the flow rate at STP, *T* is the chamber temperature, T_0 is 273.15 °K, c_{gas} is the concentration coming from the gas cylinders and $V_{chamber}$ is the chamber volume. It was assumed that the pressure in the lines and the chamber did not change significantly. Therefore the flow rates only had to be corrected to the chamber temperature, which on average was 23.5 °C prior irradiation experiments.

$$c_{chamber} = c_{gas} \times \frac{t \times Q \times \frac{T}{T_0}}{V_{chamber}} \tag{4}$$

Similarly, correcting the flows of the other MFCs from STP to chamber operation temperature was achieved by applying the temperature coefficient T/T_0.

2.3 Liquid sample injection system

Unlike propene and NO_x, most sample compounds of interest are liquids. Therefore the manifold could not be used directly to inject and analyse the photochemical transformation of e.g. *m*-xylene or MEA (**Sections 2.5.4** and **4.1**). Instead, they are injected using glassware specifically designed for the introduction of such compounds to the chamber, as illustrated in **Figure 2.2**. The liquid sample is first placed onto the external wall of the internal glass tubing, before opening the valve, which allows the hot air controlled by Manifold 1 ($T_{decomp.} > T > b.p$) to transport the sample in the gas-phase into the chamber. As the sample volumes are small (10-30 µL), careful application onto the internal glass wall will lead to the liquid remaining on the walls due to surface tension. To reduce heat loss to the environment and prevent recondensation of the sample onto the glass walls, the glassware is insulated by fiberglass during the injection period, which typically lasts for 0.5-1 hour.

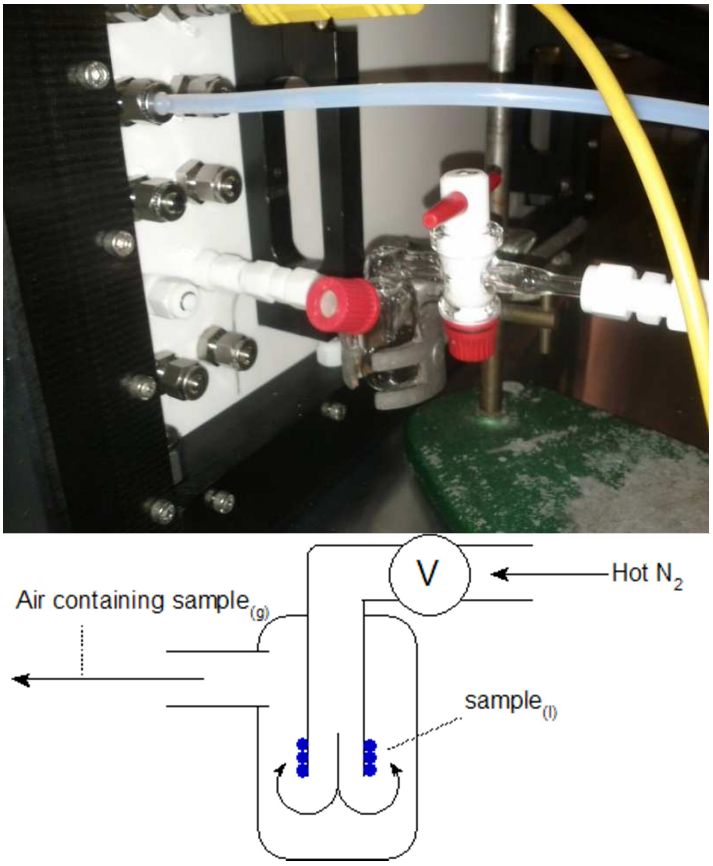

Figure 2.2: Top shows the glassware in position for liquid sample injection. Bottom is a schematic of the injection process: The liquid sample is introduced onto the walls of the internal glass tube by a syringe through a septum. The hot air ($T_{decomposition} > T > b.p$) then transports the sample in gas-phase into the chamber. When in operation, the glassware is wrapped in fiberglass to reduce heat loss to the environment.

2.4 Monitoring Instruments

There are several analytical tools attached to the chamber to monitor its internal conditions. The ozone mixing ratios are monitored by a UV photometric analyser (TES 400E).

NO, NO_2 and NO_x mixing ratios are measured by a chemiluminescence analyser (Ecotech EC 9841). Prior to major experiments, it is calibrated by passing 300 ppbv of a certified mixture of NO in N_2 (100 ppmv, BOC gases) through the analyser. The data logger returns the mixing ratios for NO, NO_2 and NO_y. NO_y is the signal for all detectable species, which include PANs, HNO_3, HNO_4, HONO, NO_3, N_2O_5 and $RONO_2$ as well.

The photochemical reaction processes will be monitored by long-path (~160 m) FTIR spectroscopy (Thermo Nicolet iS50 with a MCT detector). For this work, the FTIR was not capable of producing quantifiable data, as the long-path beam had not been aligned perfectly to the mirrors.

The internal and external chamber temperatures were measured using K-thermocouples, and the RH was measured using a calibrated humidity/temperature meter (Center 313).

Particle number concentration and size distribution were collected by a scanning mobility particle sizer (SMPS) consisting of an electrostatic classifier (TSI 3080). This instrument selects particles based on their electrical mobility, which is dependent on particle diameter. Particles between 14.6 and 661.2 nm were scanned by the classifier with a 0.071 cm impactor jet before being introduced to a condensation particle counter (TSI 3776, CPC), where they were optically detected by growing particles in butanol vapour.

2.5 Chamber characterisation

Smog chambers provide a platform to conduct controlled experiments without the complication of meteorology, emissions and mixing effects. As the environments in the chambers are an artificial construct, it is crucial to undertake characterisation experiments in order to produce good models and compare these to real world situations. Previous publications have shown a range of chamber auxiliary reaction mechanisms, which have to be taken into consideration for a full characterisation of the chamber [58-60]. **Table 2.2** summarises some of these mechanisms and indicates whether they have been quantified in this work.

Table 2.2: Auxiliary mechanisms for chamber-dependent reactions, modified from Hynes *et al* [58]

Reaction	Quantified	Parameter	Uncertainty
O_3 → wall	Yes	5.61×10^{-7} s^{-1}	6.6×10^{-9} s^{-1}
Aerosol → wall	Yes	-5.11×10^{-6} s^{-1} to 2.72×10^{-5} s^{-1}	See **Table xI.1** in Appendix I
hv + wall → HONO	No	—	—
NO_2 → 0.5 HONO + 0.5 wall-HNO_3	No	—	—
N_2O_5 + H_2O → 2 wall-HNO_3	No	—	—
Wall-HNO_3 + *hv* → OH + NO_2	No	—	—
HNO_3 → wall-HNO_3	No	—	—
NO_2 → wall	No	—	—
$[HONO]_0$	Yes[a]	< 0.1 ppbv	—

[a]based on previous experience [57]

2.5.1 Propene/NO_x experiments

When the construction of the chamber was close to completion, one of the first experiments in the commissioning stage was to perform propene/NO_x experiments. The photooxidation of propene alone does not yield any particles [61], as the break-down and transformation products are too high in volatility to undergo particle formation or condensation. If there is sufficient residual reactive material within the chamber, particle formation will be observed. Therefore this is a useful protocol to both determine the cleanness of the chamber, but also to remove contaminants or residuals from previous experiments, as depicted in **Figure 2.3**. **Table 2.3** summarises the performed propene experiments.

Table 2.3: Summary of propene/NO$_x$ experiments

Exp.	Duration^a / h	NO / ppbv	Propene/ ppbv	Max particle count / # cm^{-3}	Maximum particule volume / µm^3 cm^{-3}
PN 1	5.77	194	483	26577.23	4.17×10^{-1}
PN 2	6.71	48.5	121	7032.00	3.84×10^{-1}
PN 3	8.14	48.8	182	3733.25	6.73×10^{-1}
PN 4	7.21	48.8	182	3600.77	1.27×10^{0}
PN 5	6.80	48.8	182	2536.48	2.64×10^{-1}
PN 6	6.74	48.8	182	263.26	9.72×10^{-2}
PN 7	5.67	48.8	182	412.28	2.98×10^{-1}
PN 8	6.91	48.8	182	137.79	1.55×10^{-2}
PN 9	5.38	48.8	182	248.97	8.64×10^{-2}
PN 10	5.40	48.8	187	48.04	4.92×10^{-1}
PN 11	7.56	48.8	182	6204.83^b	2.98×10^{-1}
PN 12	3.36	48.8	182	13.28	2.06×10^{-1}

^{a}From "lights on" until last data point from SMPS (therefore includes start of flushing). ^{b}Performed after MEA injection

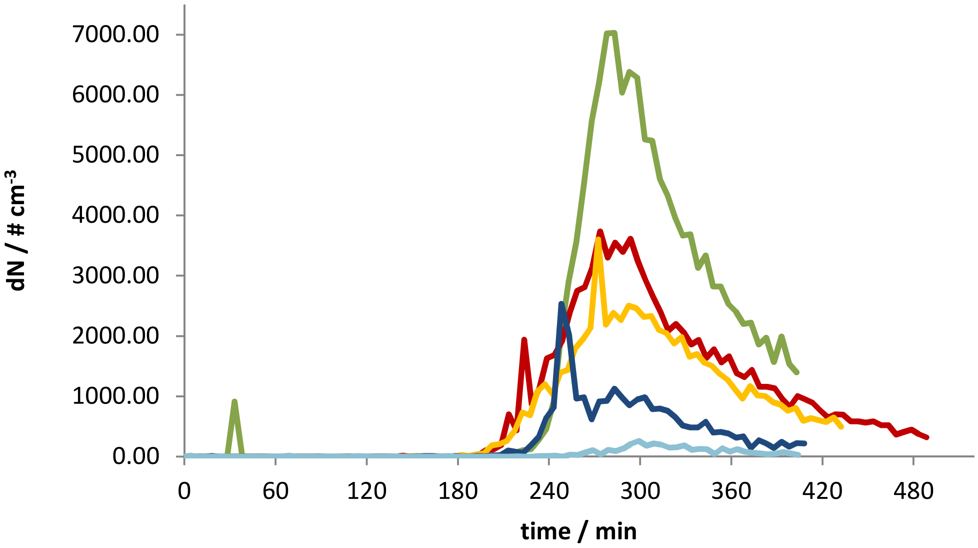

Figure 2.3: Comparison of particle formation during propene/NO$_x$ cleaning runs in Experiments PN 2-6. Green is Exp. 2, red Exp. 3, yellow Exp. 4, dark blue Exp. 5 and light blue Exp. 6. The zero-point is defined by turning on the UV-lights, whereas the decline of particle numbers around 300 min is the moment when chamber flushing was initiated.

2.5.2 NO_2 photolysis rates

For indoor chamber experiments, blacklights and not the Sun are the source of UV light. Therefore the NO_2 photolysis coefficient has to be measured, as it will differ from ambient conditions. The resulting coefficient is a measure of the total light intensity output of the chamber and is subsequently utilised to correct chamber models to ambient conditions. Additionally, the photolysis rates of other species can be determined relative to this coefficient from known light emissions spectrum and known wavelength-dependant absorption and quantum yield dissociation rates for each species of interest.

NO_2 photolysis rates were measured by steady state actinometry for four light settings [62]: all lights, half of both types, BLBs only, and UFBLs only. This method involved injecting 209 ppbv of NO_2 from a certified NO_2/He mixture (0.4 %, BOC Gases) into the chamber, followed by irradiation. As illustrated in **Figure 2.4**, by continuously monitoring the NO, NO_2 and O_3 concentrations during the established steady state, the photolysis rate coefficient, J_{NO_2} was calculated by using following equation,

$$J_{NO_2} = \frac{k_{NO+O_3} \times C_{O_3} \times C_{NO}}{C_{NO_2}}, \tag{5}$$

which is derived from **Reactions 1.1-1.3** (**Section 1.8**). The concentrations are measured in molecules cm^{-3}, while k_{NO+O_3} is empirically determined to be $2.07 \times 10^{-12} \times e^{(-1400/T)}$ [63]. On average, each steady state was monitored for an hour. J_{NO_2} was calculated for each data point recorded 10 min after the lights had been switched on, ensuring that a steady state had been achieved. The conversion of mixing ratio to concentration and the value of k_{NO+O_3} are temperature dependant. The chamber temperature was logged during the experiments. It is assumed that no significant changes in pressure occur during the experiment. In a final step the $J_{NO_2(t)}$ were averaged to give rise to the values presented in **Table 2.4.** The values for the averages (avg) and the standard deviations were obtained by pooling the data of the two experiments.

Table 2.4: Experimental results for NO_2 photolysis rates

Exp	J_{NO2} All / min^{-1}	J_{NO2} Half / min^{-1}	J_{NO2} BLB / min^{-1}	J_{NO2} UFBL / min^{-1}
N1	0.490 ± 0.033	0.279 ± 0.016	0.346 ± 0.022	0.241 ± 0.015
N2	0.534 ± 0.035	—	0.358 ± 0.025	0.246 ± 0.018
avg	0.512 ± 0.027	0.279 ± 0.016	0.352 ± 0.013	0.237 ± 0.009

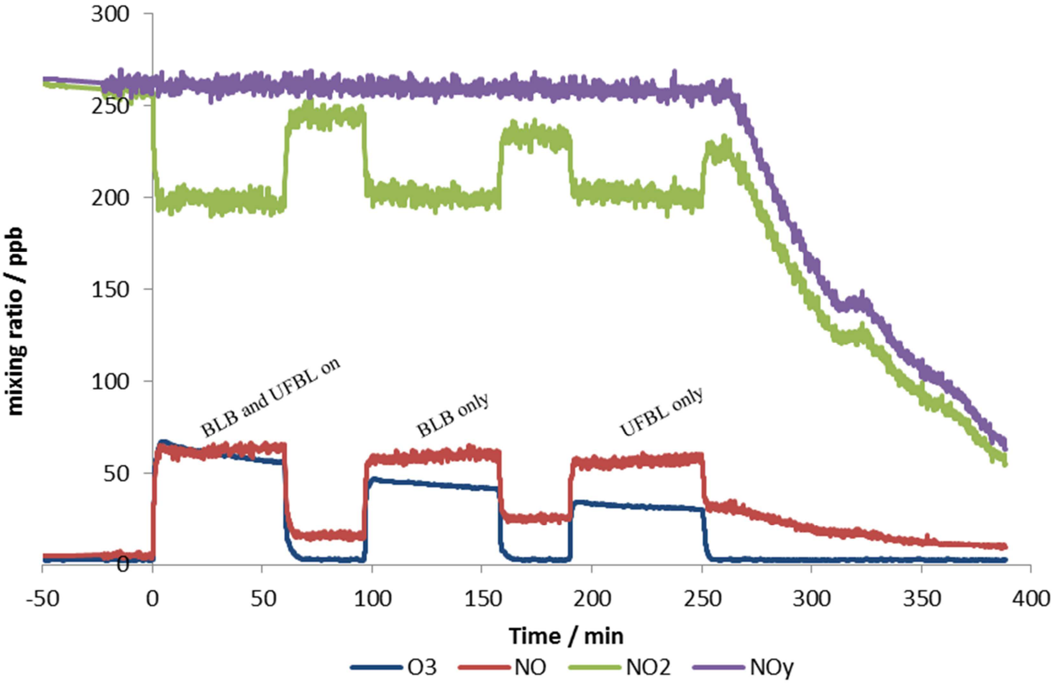

Figure 2.4: O_3 and NO_x mixing ratios logged by the respective analysers for photolysis experiment N2

2.5.3 Wall loss of O_3

One of the identified auxiliary mechanisms is the deposition of ozone to the walls. This becomes important for longer experiments, which require ozone concentrations for kinetic modelling, as then they have to corrected for the ozone loss to the walls. The wall loss of O_3 proceeds in a first order reaction, therefore by injecting a known starting amount and monitoring the ozone decay, the rate loss constant can be evaluated. Three ozone loss experiments were conducted: two test experiments and a third one, which quantified the wall loss over four days.

For the final ozone experiment (Exp. 19), ozone was generated by a small cell containing a mercury lamp which operates at 254 nm and photolyses oxygen to ozone from clean air passing through the cell. After 1 hour 40 minutes, ~134 ppbv ozone had been injected into the chamber and was left to rest for 90 hours. The monitoring devices were switched off after 4.5 hours after the injection and switched on for the fourth day to finish the wall loss observations. **Figure 2.5** illustrates the decline of ozone throughout the four day period, plotted as the natural log of concentration against time. The resulting rate loss constant is $(5.6112 \pm 0.0011) \times 10^{-7}\ s^{-1}$. This value is both lower than the reported value of $\sim 1 \times 10^{-6}\ s^{-1}$ by Hynes *et al.* [58] for the first month of chamber operations and the values presented in **Table 2.5**. It is expected that the ozone wall loss for this chamber will decrease after some years of operations, as Hynes *et al.* observed their wall loss rate drop by ~80 % to ~2 × 10^{-7} s^{-1} after three years.

Table 2.5: O3 wall loss rates from other chambers

Publication	Wang *et al.* (2014) [64]	Grosjean (1985) [46]	Bloss *et al.* (2005) [59]	Metzger *et al.* (2008) [27]	Current work
Chamber size / m^3	30	60	200	27	24.7
Wall loss rate / s^{-1}	2.18 × 10^{-6}	0.8-5 × 10^{-6}	3 × 10^{-6}	4 × 10^{-6}	(5.6112 ± 0.0011) × 10^{-7}

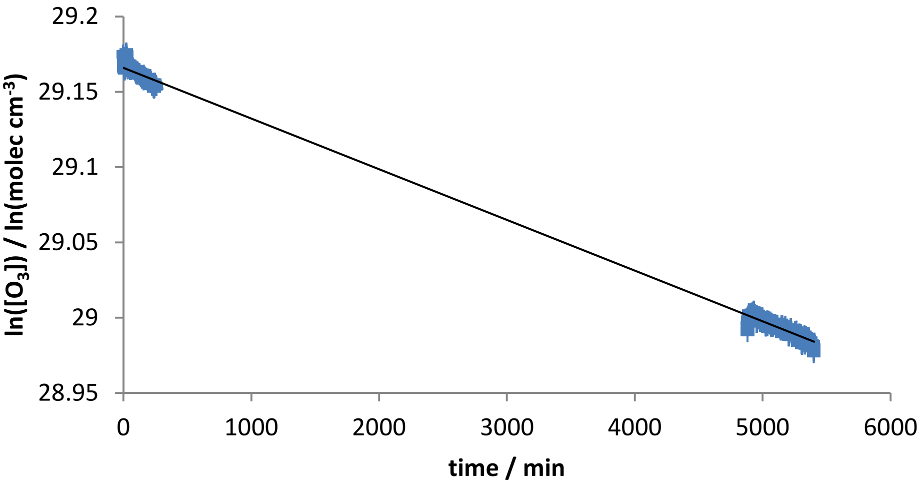

Figure 2.5: Natural log of ozone concentration plotted against experimental time (minutes) to obtain wall loss rate coefficient for experiment 19. Regression statistics are a slope of -3.367 × 10^{-5} ± 6.6 × 10^{-9} min^{-1}, while the intercept is 2.917 × 10^{1} ± 2.7 × 10^{-5}, R^2 is 0.9990 and the residual sum of squares is 1.653 × 10^{-1} min^{-2}

2.5.4 Particle wall loss

Loss of particles to the reactor walls is a common phenomenon for all atmospheric chambers and is influenced by diffusion, chamber shape and the charged walls [64, 65]. Various studies have analysed the influence of these variables on particle deposition, such as the rate loss of charged and neutral particles in electrically charged chambers [66] or the deposition rate as a function of chamber shape [67].

Based on a report for the particle loss to the walls for CSIRO's second generation chamber [65], the most significant factors to aerosol loss are particle size, stirring intensity within the chamber, electrical charging, vessel shape and temperature differences within the chamber. For the current chamber, the two most prominent factors are stirring and particle size, as the rectangular shape of the vessel is easily accounted for and there are no significant temperature changes within the chamber. As Teflon is not completely inert, electrical charging might contribute slightly to the wall loss rate. However, compared to the glass walls of Seinfeld and Crump's chamber where the work on particle loss was initiated, the significance of this factor is highly reduced [65, 67].

Through the work of Fuchs [68], Takekawa *et al.* [69] and Wang *et al.* [64] it has been established that the particle wall loss rate is proportional to particle concentration and depends on particle size. Therefore the wall loss rate can be determined by first-order kinetics as stated in **Equation 6**, where $N(d_p, t)$ is the particle number concentration, d_p is the diameter midpoint of the "particle bin", and β is the wall loss coefficient [70].

$$\frac{dN(d_p,t)}{dt} = -\beta(d_p) \times N(d_p, t), \tag{6}$$

This equation can be integrated and rewritten to produce **Equation 7**, which allows to plot the natural logarithm of the particle count versus time, so β can be determined from the slope.

$$\ln\left(N(d_p, t)\right) = -\beta(d_p) \times t + k \tag{7}$$

For this experiment, *m*-xylene (11.3 mg, 0.000106 mol, 104 ppbv) was injected for 1 hour 15 minutes into the chamber at 2.5 L min^{-1} and a line temperature of 57 °C. At the time of injection the RH of the chamber was 7.2 % and the temperature was 23.4 °C. After allowing the *m*-xylene to mix through diffusion for an hour, as the zero air plant was offline due to maintenance, 30 ± 1 ppbv NO was injected into the chamber and allowed to mix for a further hour. Next the UV-lights were turned on for 6 hours to promote particle formation through photooxidation. After approximately 40 minutes particle formation was observed and within the first hour maximal particle count was recorded. During the 6 hour irradiation, the particle count started to decrease, while the particle volume increased. This is to be expected, as smaller particles grow into particles that reside in the *accumulation mode* by condensation and to a small degree coagulation. After turning the UV-lights off, the analytical instruments and the injection lines were disconnected from the chamber before sealing the inlets.

In the morning only the SMPS was reconnected to the chamber in order to minimise particle loss through other outlets. When comparing the first measurement on Day Two to the last measurement on Day One, it became apparent that further particle growth had occurred during the night. On Day One the highest particle count was for the 101.8 nm bin, while on Day Two the highest count had shifted to the 117.6 nm bin. This growth could be a consequence of SVOCs non-reversibly partitioning into the aerosol phase in the dark or a shift of the equilibrium between evaporation and repartitioning of SVOCs to the particle phase. Therefore the particle wall loss rate was calculated for the data points collected on Day Two only, as it was assumed that by this time there was no significant particle growth.

By using the first-order kinetics approach described earlier, the wall loss rate for the particles with diameter midpoints of 51.4 nm to 181.4 nm were determined. Bins containing lower or higher particle diameters showed inconsistent and insufficient particle counts during the analysed time frame. The results are presented in **Table 2.6**.

Table 2.6: Calculated wall loss rates *β* for particles in the range of 51.4 nm and 181.1 nm using a first-order kinetics approach, as established by Wang *et al* and others [64, 69].

Bin / nm	51.4	53.3	55.2	57.3	59.4	61.5
Rate / min^{-1}	6.235×10^{-4}	-3.066×10^{-4} [a]	1.517×10^{-3}	1.358×10^{-3}	8.722×10^{-4}	1.293×10^{-3}
Bin / nm	63.8	66.1	68.5	71	73.7	76.4
Rate / min^{-1}	1.631×10^{-3}	1.442×10^{-3}	1.304×10^{-3}	1.221×10^{-3}	1.513×10^{-3}	1.244×10^{-3}
Bin / nm	79.1	82	85.1	88.2	91.4	94.7
Rate / min^{-1}	1.465×10^{-3}	1.107×10^{-3}	1.151×10^{-3}	1.022×10^{-3}	1.115×10^{-3}	9.735×10^{-4}
Bin / nm	98.2	101.8	105.5	109.4	113.4	117.6
Rate / min^{-1}	1.080×10^{-3}	9.539×10^{-4}	1.022×10^{-3}	7.696×10^{-4}	8.176×10^{-4}	9.554×10^{-4}
Bin / nm	121.9	126.3	131	135.8	140.7	145.9
Rate / min^{-1}	8.036×10^{-4}	6.580×10^{-4}	6.642×10^{-4}	6.609×10^{-4}	6.468×10^{-4}	4.689×10^{-4}
Bin / nm	151.2	156.8	162.5	168.5	174.7	181.1
Rate / min^{-1}	5.451×10^{-4}	5.845×10^{-4}	2.170×10^{-4}	3.996×10^{-4}	2.261×10^{-4}	3.196×10^{-4}

[a] negative value indicates growth instead of decay

Next, the particle wall loss was simulated using the new *β*-values and the values from the second generation chamber [65]. Both were compared to the experimental data. As anticipated, when compared the new wall loss rates simulated the particle loss better than the old rates, especially for particles with larger diameters, as shown in **Figure 2.6** and **Figure** 2.7.

As the SMPS-CPC settings used for the determination for the particle wall loss rate were not sensitive enough for smaller particles, in future experiments one should consider extending the acquisition time to increase accuracy at smaller numbers of particles. Furthermore, in order to determine the wall loss rates for the remaining bins, another compound should be used that produces sufficient particles in the range of 181.1-661.2 nm. Additionally, the current β-values should be tested in other particle loss experiments to determine their versatility for other systems.

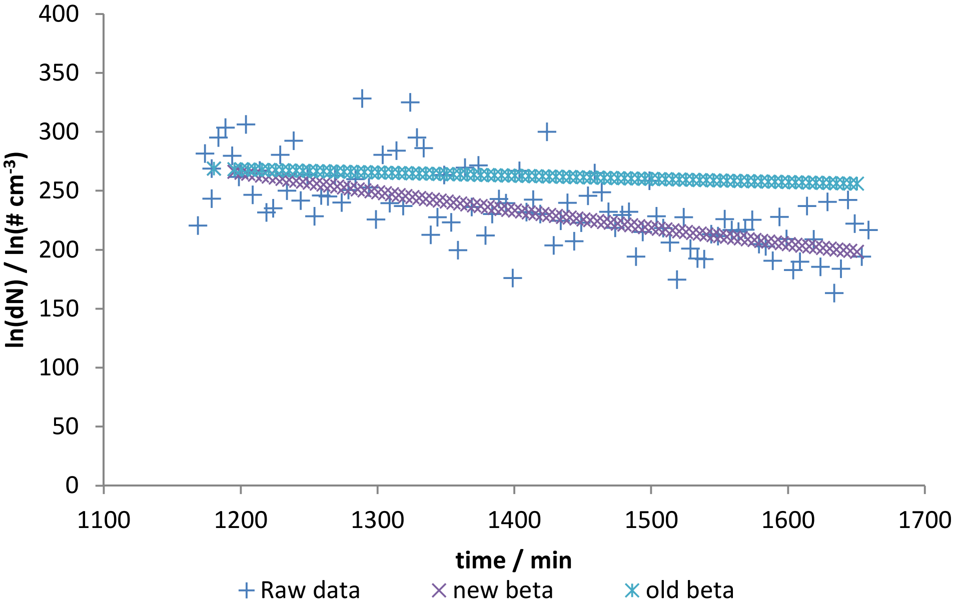

Figure 2.6: Particle wall loss for particles in the 140.7 nm bin simulated with new and old β-values and compared to raw data

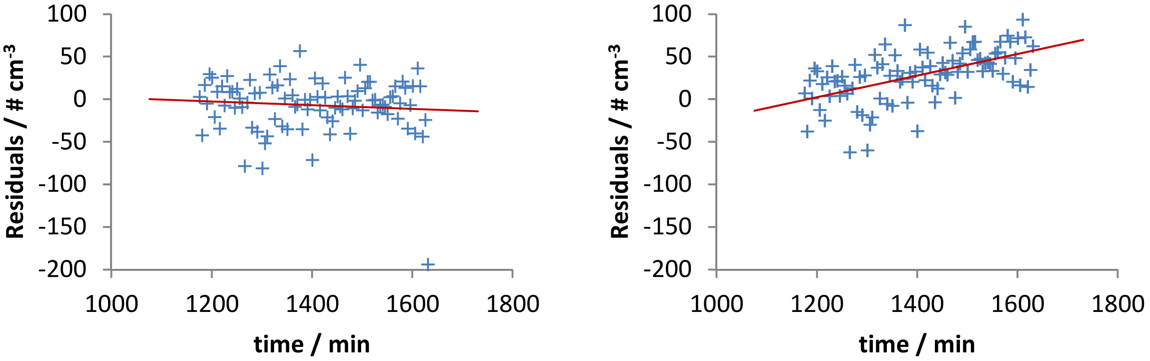

Figure 2.7: Residual plots for new $\beta_{140.7nm}$-value (left) and old $\beta_{140.7nm}$-value (right) simulations from Figure 2.6

In summary, this experiment was successful in updating the wall loss coefficients for a portion of the particle bins analysed by the new SMPS-CPC and therefore corrections for particle loss can be made for these bins in future experiments. However, as stirring intensity is one of the crucial variables influencing particle wall loss, these experiments should be postponed and repeated once the mixing inside the chamber has been improved by e.g. installing fans inducing the Teflon walls to oscillate.

2.5.5 Outstanding characterisations

As shown in **Table 2.2**, there are still several auxiliary reaction mechanisms, which have to be quantified for the new chamber. These will be addressed within the coming months.

- The wall production of HONO can be measured by performing a clean irradiation experiment and subsequently modelling the O_3 and NO_x concentrations and incorporating HONO concentrations when available, as done by Rohrer *et al* [71].
- The background concentration of hydrocarbons can be determined either by modelling the results obtained for a clean air irradiation experiment [58], or using an FID.
- The hydrolysis of NO_2 to HONO and absorbed NO_x and the gas-phase hydrolysis of N_2O_5 to adsorbed HNO_3 can be determined through simulations using generated experimental data from clean air, low NO_x-air, CO-NO_x-air or CO-air irradiation experiments [58]. An alternative method is to use values from previous publications, such as Bloss *et al.* or Hynes *et al.* [58].
- NO, NO_2, propene and HNO_3 wall loss rates have to be determined experimentally. The NO, NO_2, HNO_3 and propene wall loss coefficients can be estimated in the same manner as ozone deposition (**Section 2.5.3**).

2.6 Further chamber improvements

There are three major improvements that can be made to the current chamber. First, the long-path FTIR still has to be aligned properly. As the aimed path length for the IR beam is ~160 m, it remains a great challenge to precisely align the beam with the mirrors to get a signal which allows quantifications of gas species *in situ*. Secondly, mixing of the introduced species currently relies on either diffusion or by introducing short, strong pulses of pure air. In future, it is intended to install fans below the chamber, which will induce oscillation in the Teflon walls, enhancing and ensuring continuous mixing throughout experiments. Finally, the current zero air plant does not have a functioning dehumidifier. For later experiments, especially in the summer months, where humidity will rise and reach critical levels for amine irradiation experiments, it will be a necessity to have a functioning dehumidifier to control the chamber's internal relative humidity. Previous experiments on amine systems have shown a significant sensitivity to humidity [72]. Currently arrangements are being made, so that humidity becomes controllable in the coming months.

Chapter 3. Particle-into-Liquid sampler and Ion Chromatography

3.1 Particle-into-Liquid Sampler

The Particle-into-Liquid Sampler (PILS) used for this project was obtained from Metrohm AG and is based on the improved version described in detail by Orsini *et al*. [73]. In brief, the principle of a PILS is to collect particulate matter and dissolve it into ultra-pure water yielding a solution containing the water-soluble components of aerosol, which in turn can be quantified by methods such as, but not limited to, IC, LCMS and EC/OC-analysers [73, 74].

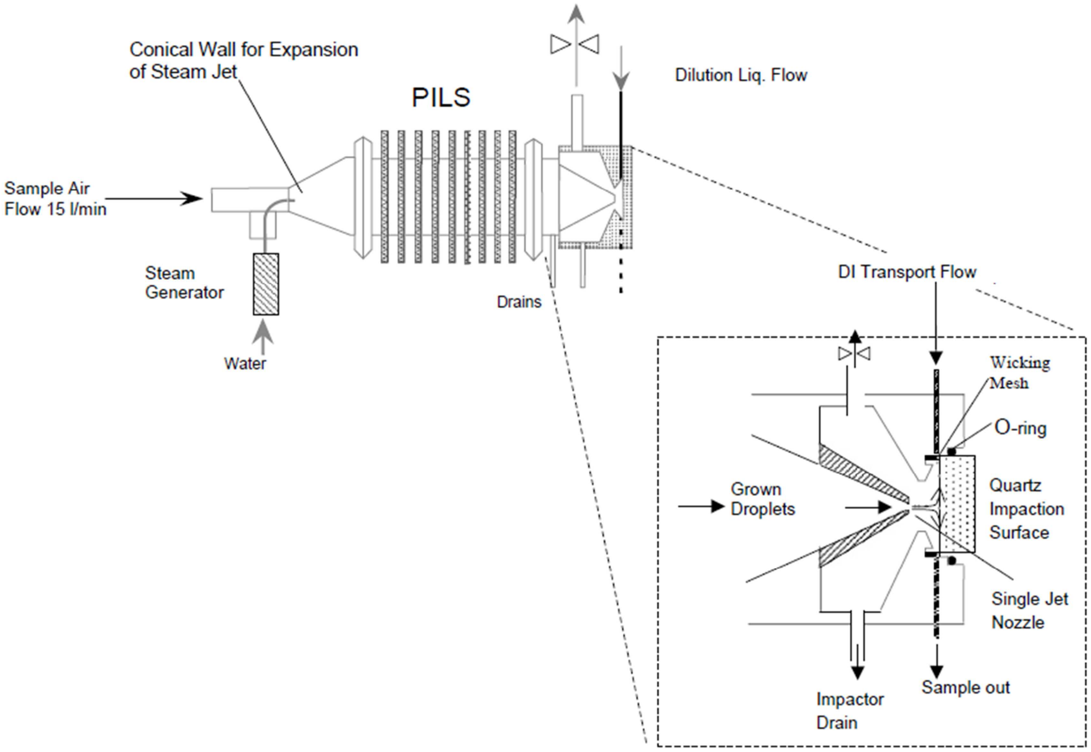
Conical Wall for Expansion of Steam Jet
PILS
Dilution Liq. Flow
Sample Air Flow 15 l/min
Steam Generator
Water
Drains
DI Transport Flow
Wicking Mesh
O-ring
Quartz Impaction Surface
Grown Droplets
Single Jet Nozzle
Impactor Drain
Sample out

Figure 3.1: Schematic of PILS, adopted from Orsini *et al* [73]

Growing water droplets from particulate matter is achieved by first mixing the air flow (16.7 L min^{-1}) containing aerosol from the chamber with a smaller flow of 150 °C ultra-pure water steam, as shown in **Figure 3.1**. The cooler air stream then rapidly cools the water steam adiabatically and generates to a supersaturated environment, in which water droplets with diameters larger than 1 µm grow from aerosol particles. The droplets are then collected by a quartz impactor plate and then transported to the online analyser by a slow flow of deionised water spiked with an internal standard. Due to the correspondence between the CSIRO PILS instrument and that described in Orsini *et al*, it is assumed that the CSIRO PILS has a collection efficiency of 97 % for particles ranging from 30 nm to 10 µm, and an upper size limit of 11 µm.

3.2 Ion chromatography

The IC-system is a 850.3030 Professional IC Ancart MCS obtained from Metrohm AG. It consists of two 250 µL sample loops, one for each ion chromatograph column, two columns, a thermostat, two IC conductivity detectors (Metrohm) and a set-up for anion suppression. The original cation column was a Metropsep C4 100/4.0 and run with 1.7 mmol L^{-1} HNO_3 / 0.7 mmol L^{-1} dipicolinic acid, while the anion column is a Metrosep A Supp 100/4.0 and 3.2 mmol L^{-1} sodium carbonate / 1.0 mmol L^{-1} sodium bicarbonate is the eluent. The anion suppression is achieved by the Metrohm Suppressor Module, in which the anion's counter ions are replaced by hydrons, increasing the sensitivity of the subsequent conductivity analysis.

Modifications to the instrument were made to achieve better separation for amines by installing a Metrosep C4 250/2.0 cation column. This did not require a change in eluent. Improvements to anion separation aimed at organic anions were attempted by the installation of a different column (Metrosep A Supp 15 250/4.0), but not pursued due to difficulties in achieving the required operating temperature for the anion column.

3.3 Calibration experiments

Quantitative and qualitative analysis required calibration of the IC hardware and software for particular species of interest. Retention times for a selection of prominent organic and inorganic ions were determined by direct injection into the IC, to allow identification of most peaks from the conductivity analysis for each sample. Additionally, ions of higher significance, such as lithium (internal standard), MEA (amine of interest), ammonia (product of MEA photolysis) and nitrate (product of photolysis) were calibrated in order to quantify changes of aerosol composition during the course of the photolysis reactions. **Table 3.1** summarises all retention times available for the cations (long column) and anions (short column) analysed during the project.

Table 3.1: Retention times for cations and anions analysed during the project. Cations were injected onto a Metrosep C4 250/2.0 at 0.2 mL min^{-1} and 30 °C and anions onto a Metrosep A Supp 100/4.0 at 0.7 mL min^{-1} and 30 °C. Abbreviations used: Ac – acetate, Gly – glycolate.

Cations							
Species	Li^+	Na^+	NH_4^+	MEA^+	K^+	Ca^{2+}	Mg^{2+}
Retention time / min	9.88	11.88	12.98	14.44	16.42	36.26	44.27
Peak width at half max. / min	0.20[a]	0.21[a]	0.22[b]	0.26[a]	0.28[a]	0.79[a]	1.06[a]

Anions										
Species	F^-	Gly	Ac	Cl^-	NO_2^-	Br^-	NO_3^-	SO_4^{2-}	PO_4^{3-}	$C_2O_4^{2-}$
Retention time / min	3.41	3.56	3.87	4.60	5.28	6.47	7.25	9.60	10.81	12.43
Peak width at half max. / min	0.12[b]	0.17[a]	0.24[a]	0.13[b]	0.22[a]	0.16[b]	0.18[b]	0.24[b]	0.24[b]	0.31[a]

[a]injection concentration 100 µg L^{-1}. [b]injection concentration 50 µg L^{-1}

3.3.1 Cations

3.3.1.1 Lithium, Sodium, Potassium, Calcium and Magnesium

These cations were calibrated by injecting serial dilutions from a 10.0 mg kg^{-1} ± 0.2 % multi ion standard (Fluka), as shown in **Table 3.2**. For the dilutions precision micro pipettes and MilliQ water (R = 18.5 Ω) were used. Due to long run times (50 minutes), only duplicates were collected for this calibration

Table 3.2: Dilutions used for cation calibration for IC system

Sample	1	2	3	4	5
Concentration	1.0 µg L^{-1}	5.0 µg L^{-1}	10 µg L^{-1}	25 µg L^{-1}	50 µg L^{-1}

During the injections traces of ammonia were detected, which were introduced during sampling handling. The most important component of the multi-ion calibration is lithium, as it is required for the quantification of the internal standard in aerosol-water samples. **Figure 3.2** shows the calibration plot for lithium, while **Table 3.3** summarises the calibration data for the all species.

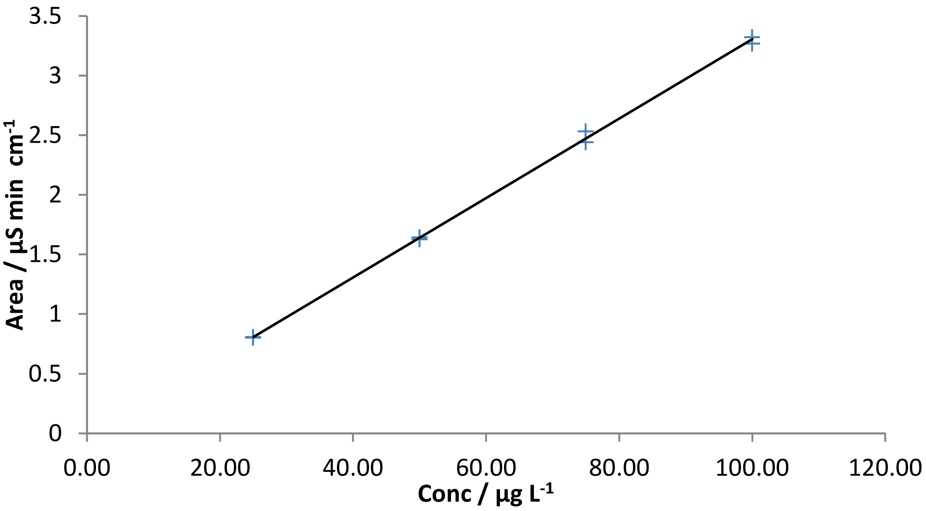

Figure 3.2: Calibration plot for lithium. Statistical analysis from a linear regression yields that the slope is 0.03330 ± 0.00042 µS min L cm^{-1} µg^{-1}, while the intercept is -0.025 ± 0.029 µg L^{-1}, R^2 is 0.9990 and the residual sum of squares is 0.006616 µS^2 min^2 cm^{-2}.

Table 3.3: Statistical data for the cation calibrations from multi-ion injections

Species	Lithium	Sodium	Potassium	Calcium	Magnesium
Slope / µS min L cm^{-1} µg^{-1}	0.03330 ± 0.00042	0.0140 ± 0.0019	0.00666 ± 0.00090	0.0139 ± 0.0022	0.01763 ± 0.00031
Intercept / µg L^{-1}	-0.025 ± 0.029	-0.10 ± 0.13	-0.041 ± 0.061	-0.22 ± 0.15	-0.088 ± 0.021
R^2	0.9990	0.9023	0.9019	0.8646	0.9982
SS$_{resid}$ / µS^2 min^2 cm^{-2}	0.006616	0.1318	0.03012	0.1895	0.003496

The calibration data for sodium, potassium and calcium are not fully satisfactory when taking the correlation factors and the residual sum of squares into consideration. Both sodium and potassium were later identified as contaminants that were most likely introduced during sampling handling (see **Sections 3.3.1.2** and **Section 3.3.1.3**). Therefore it is plausible that random amounts of these species have led to the reduction of data quality. However, calcium was not observed to be introduced during sampling handling. Consequently, when deemed necessary to quantify these species in future, it is strongly recommended to do a third run to improve the plots for sodium and potassium by removing suspected outliers (see **Figure xI.2** in Appendix I) and to perform a new calibration for calcium, potentially using a different standard.

3.3.1.2 Ammonium

Ammonium was calibrated in the same manner as the multi-ions. Serial dilutions were prepared from a 1000 ± 4 mg L^{-1} standard (NH_4Cl, *Trace*CERT®, Fluka), as shown in **Table** 3.4.

Table 3.4: Dilutions used for ammonium calibration for IC system

Sample	1	2	3	4	5
Concentration	1.0 µg L^{-1}	5.0 µg L^{-1}	10 µg L^{-1}	25 µg L^{-1}	50 µg L^{-1}

Before starting the analysis of the serial dilutions, a blank sample was run to determine contaminants which had been introduced during sample preparation. This injection yielded traces of ammonium, sodium and potassium. This blank was then used to correct the ammonium concentration by 0.019 µS min cm^{-1} for the further injections under the assumption that the degree of contamination stayed constant. This correction shifted the intercept to the origin within uncertainty.

Due to time constraints, each concentration was only analysed once. When time allows, it is recommended to expand the analysis to triplicates to have a higher confidence in the calibration data. However, as the current project was focused on integrating the PILS with the chamber operating system, a single determination was sufficient to provide preliminary data. Furthermore, if possible, it should be investigated whether the assumption that the introduced ammonium during sample preparation remains constant. **Figure 3.3** presents the calibration plot for ammonium.

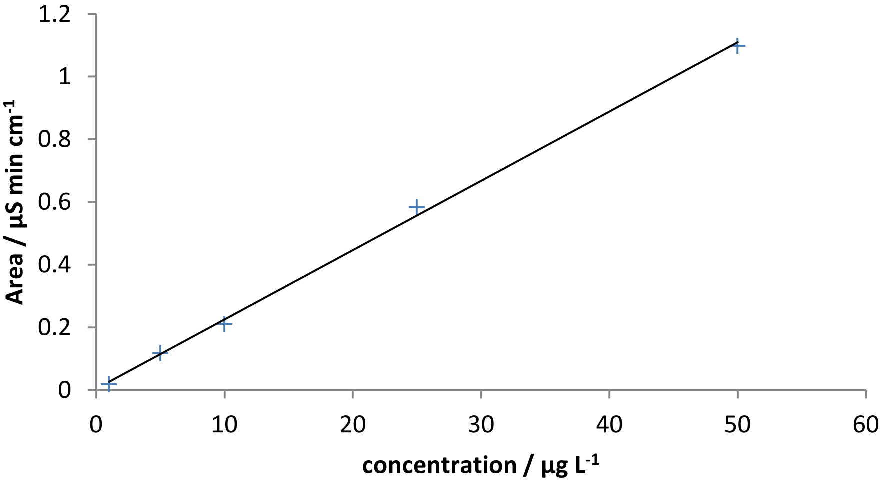

Figure 3.3: Calibration plot for ammonia. Statistical analysis from a linear regression yields that the slope is 0.02211 ± 0.00048 µS min L cm^{-1} µg^{-1}, while the intercept is 0.004 ± 0.012 µg L^{-1}, R^2 is 0.9986 and the residual sum of squares is 0.001081 µS^2 min^2 cm^{-2}.

3.3.1.3 Monoethanolamine (MEA)

A MEA stock and subsequent dilutions were prepared from the pure compound (Aldrich). The first two dilutions were done by mass to mass, while the serial dilutions thereafter were done in volumetric ratios, as the concentration of MEA was considered low enough to no longer alter the density of the liquid. **Table 3.5** summarises the stock sample preparation. The dilutions used for calibration were spiked with a ~0.002 mmol L^{-1} HNO_3 solution, which was prepared from trace-metal analysis grade nitric acid (Sigma). Due to time constraints, each concentration was only analysed in duplicates. **Figure 3.4** shows the calibration plot for MEA

Table 3.5: Preparation of MEA stock solution (1.1 mg L^{-1}) from pure MEA.

a)	MEA solution[a] / g	H_2O / g	Total Mass / g	m:m / $g_{solute}/g_{solvent}$	Concentration / g kg^{-1}
Solution 1	0.0145	1.0200	1.0345	0.0142	14.2
Solution 2	0.0082	1.0528	1.0610	0.0078	0.11

[a] pure MEA was used for solution 1, while solution 2 is a dilution from solution 1.

b)	MEA solution[b] / mL	H_2O / mL	Total Volume / mL	V:V / $V_{solute}/V_{solvent}$	Concentration / mg L^{-1}
Stock Solution	0.040	3.960	4.000	0.010	1.1

[b] prepared from solution 2 in table 3.5 a.

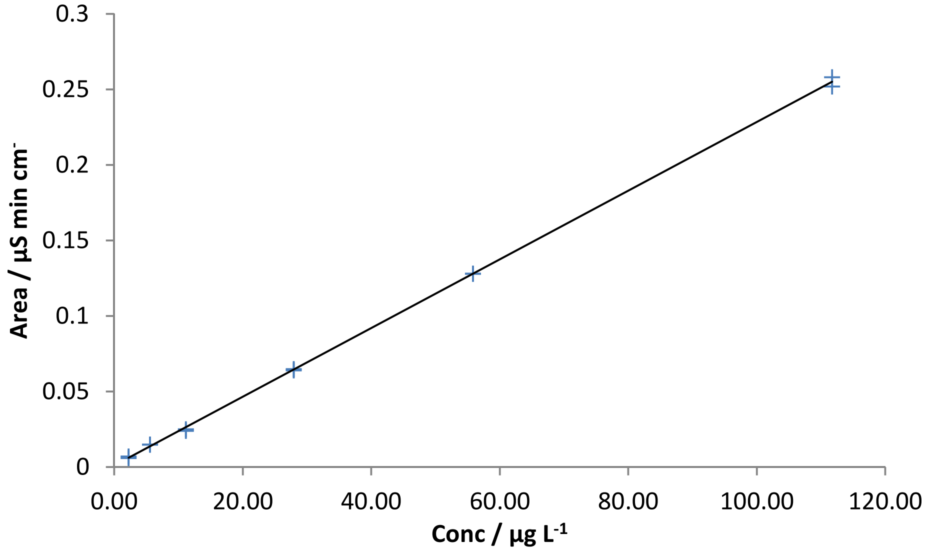

Figure 3.4: Calibration plot for MEA. Statistical analysis from a linear regression yields that the slope is 0.002273 ± 0.000013 µS min L cm^{-1} µg^{-1}, while the intercept is 0.00100 ± 0.00069 µg L $^{-1}$, R^{2} is 0.9997 and the residual sum of squares is 3.043 × 10^{-5} µS^{2} min^{2} cm^{-2}.

As with ammonium and the multi-ion injections, sodium, potassium and ammonia were the detected contaminants. As sodium concentrations seemed to rise with the MEA concentrations (see **Figure xI.3** in Appendix I), it was assumed that the majority of the contaminants were introduced in the first dilution step (solution 1). The origin of contaminants was later investigated (**Section 3.4**).

3.3.2 Anions

3.3.2.1 Bromide

Another important species to calibrate was bromide, as it is the counter ion to lithium in the internal LiBr standard. As with the cation species, serial dilutions were prepared from a 1000 ± 4 mg L^{-1} standard (*Trace*CERT®, Fluka), as presented in **Table 3.6**. Each concentration was analysed in triplicates

Table 3.6: Dilutions used for bromide calibration for IC system

Sample	1	2	3	4
Concentration	25.0 µg L^{-1}	50.0 µg L^{-1}	75.0 µg L^{-1}	100 µg L^{-1}

The data was subjected to a Grubbs test at a 95 % confidence level, as presented in **Table xI.2** in the appendix, and the outliers were rejected to yield the plot in **Figure 3.5**.

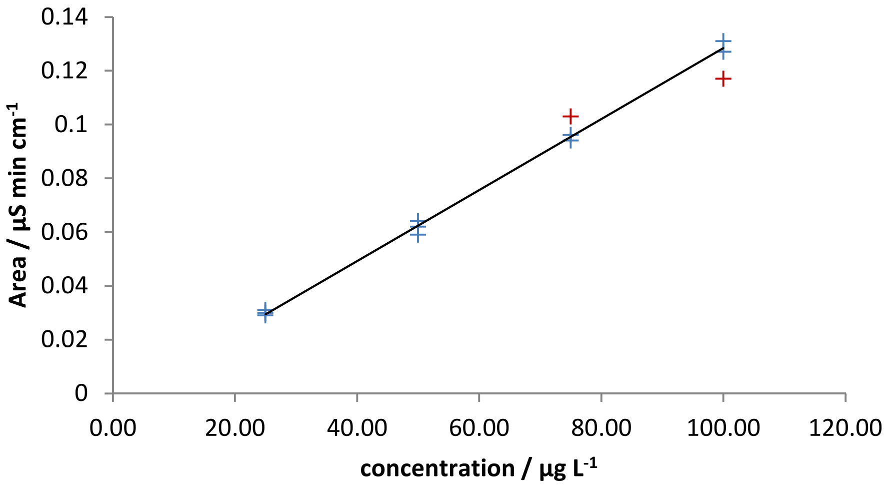

Figure 3.5: Calibration plot for bromide. The two outliers are red. The Statistical analysis from a linear regression yields that the slope is 0.001319 ± 0.000022 µS min L cm^{-1} µg^{-1}, while the intercept is -0.0036 ± 0.0014 µg L^{-1}, R^2 is 0.9978 and the residual sum of squares is 2.840 × 10^{-5} µS^2 min^2 cm^{-2}.

3.3.2.2 Nitrate

NO_x will not only act as an oxidative species, but can also be oxidized to NO_3^- and form HNO_3. Nitric acid can subsequently undergo acid-base reactions to form salt-based compounds within aerosol. Therefore following the nitrate formation during particle generating reactions is of interest, as it allows quantification of the organic and salt fractions produced during aerosol nucleation. For the calibration, nitrate dilutions were prepared from a 1000 ± 4 mg L^{-1} standard (*Trace*CERT®, Fluka), as displayed in **Table 3.7**.

Table 3.7: Dilutions used for nitrate calibration for IC system

Sample	1	2	3	4	5
Concentration	1.00 µg L^{-1}	10.0 µg L^{-1}	25.0 µg L^{-1}	50.0 µg L^{-1}	100 µg L^{-1}

The nitrate calibration was the most challenging one due to low reproducibility of concentration readings from the standards. Initially it was thought that similar to calcium and sodium, sample handling could have led to fluctuations within the standard concentrations. However, after analysing MilliQ water injected after the final standard run, traces of nitrate were still observed. This indicated that nitrate traces remained either in the external sampling line or somewhere within the sample loop of the IC apparatus. Previous to this discovery the external sample line and sample loop in the apparatus had only been flushed briefly.

Therefore for the final dilution series the external sample line was flushed continuously and the anion column was flushed in between each run. When comparing each dilution series, the final series had the best correlation coefficient and the lowest residual sum of squares (see **Table 3.8**). However, this coefficient is not enough to dismiss the other two runs. Therefore all data points were included into the calibration, except outliers which were rejected by a Grubbs test at a 95 % confidence level. The results are tabulated in **Table xI.3** in the appendix.

Despite a significant improvement of the data set after removing the two outliers, in future one should consider using the approach from the final dilution series to both improve the calibration presented in **Figure 3.6** and to examine whether the method does yield better data.

Table 3.8: Comparison of the linear regression statistics for three nitrate dilution series

Dilution series	1	2	3	Combined	Outliers removed
R^2	0.9858	0.9795	0.9945	0.9667	0.9907
$SS_{residual}$ / μS^2 min^2 cm^{-2}	0.000273	0.000739	0.000126	0.00260	0.000465

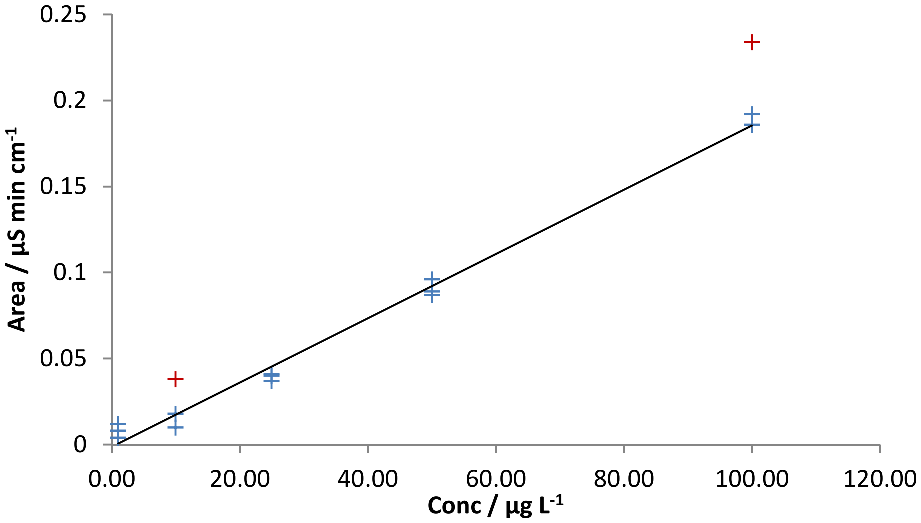

Figure 3.6: Calibration plot for nitrate. The two outliers are marked red. Statistical analysis from a linear regression yields that the slope is 0.001867 ± 0.000055 µS min L cm^{-1} μg^{-1}, while the intercept is -0.0013 ± 0.0026 µg L^{-1}, R^2 is 0.9907 and the residual sum of squares is 0.0004649 μS^2 min^2 cm^{-2}.

3.4 Contamination experiment

During the calibration experiments, it was clear that sample preparation was introducing contaminants into the standard solutions, as the analysis of bottled MilliQ water yielded only very small quantities of sodium and chloride. As a consequence, a contamination experiment was conducted to examine which containers (small and large plastic sample tubes) and transferring equipment (plastic pipette tips and glass Pasteur pipettes) were introducing the bulk of contaminants. For the experiment, MilliQ water was poured into the sample tubes either directly to test the leaching of the containers or transferred with the pipettes to examine their cleanness. **Table 3.9** below summarises the results.

Table 3.9: Results on injected samples from four sources of sample contamination. Abbreviations used: Gly – glycolate, Ac – acetate, Ox – oxalate

C1: MilliQ H_2O injected directly into small sample tubes (~15 mL)									
Species	Gly	Ac	Cl^-	NO_3^-	PO_4^{3-}	SO_4^{2-}	Na^+	NH_4^+	K^+
Area / µS min cm^{-1}	0.016	0.001	0.014	0.002	0.007	0.001	0.051	0.008	0.029

C2: Triple rinse of plastic pipette tips used for H_2O transfer								
Anions	Gly	Ac	Cl^-	Br^-	NO_3^-	SO_4^{2-}	PO_4^{3-}	Ox
Area / µS min cm^{-1}	0.315	0.030	0.180	0.001	0.094	0.001	0.194	0.024
Cations	Li^+	Na^+	NH_4^+	MEA^+	K^+			
Area / µS min cm^{-1}	0.005	1.307	0.172	0.010	0.510			

C3: Triple rinse of Pasteur pipette used for MEA transfer									
Anions	Gly	Ac	Cl^-	NO_2^-	NO_3^-	PO_4^{3-}	Ox	?	?
Area / µS min cm^{-1}	0.101	3.185	0.879	0.003	1.459	1.567	0.235	0.038	0.003
Cations	Li^+	Na^+	MEA^+	K^+					
Area / µS min cm^{-1}	0.003	14.007	0.093	0.194					

C4: MilliQ H_2O stored in ~40 mL plastic tube						
Species	Gly	Cl^-	NO_3^-	PO_4^{3-}	Na^+	K^+
Area / µS min cm^{-1}	0.006	0.003	0.001	0.001	0.031	0.012

These results indicate that the highest amounts of impurities are introduced by using a Pasteur pipette, including two unidentifiable species (marked by “?”), as their retention times did not match the database. Therefore in subsequent sample preparations Pasteur pipettes were not used. Rinsing the plastic tips for the high-precision pipette tips showed high levels of sodium and potassium. Consequentially, it was decided to rinse the tips prior to sample preparation in an attempt to reduce the transferral of inorganic ions. Satisfactory results were obtained for the small sample tubes, which were used to prepare the dilutions aeries and the large plastic tubes, which were used to store and transport larger amounts of MilliQ H_2O. Both vessels showed low levels of contaminants, with the large plastic tubes having the fewest observed species among all analysed sources. Therefore it was concluded to be safe to continue using the storage vessels, while for sample handling some minor changes were undertaken for micro pipetting.

3.5 Internal Standard

The internal standard is required to correct for dilution fluctuations when the particulate matter entering the PILS is grown to water droplets and collected by the impactor. Additionally, one can estimate the aerosol concentration inside the chamber. Both require understanding the interactions of the in- and outgoing flows of the PILS. By using the schematic presented in **Figure 3.7** and the generic formula $c_1V_1 = c_2V_2$, **Equation 11** [73] can be derived from **Equations 8-10**.

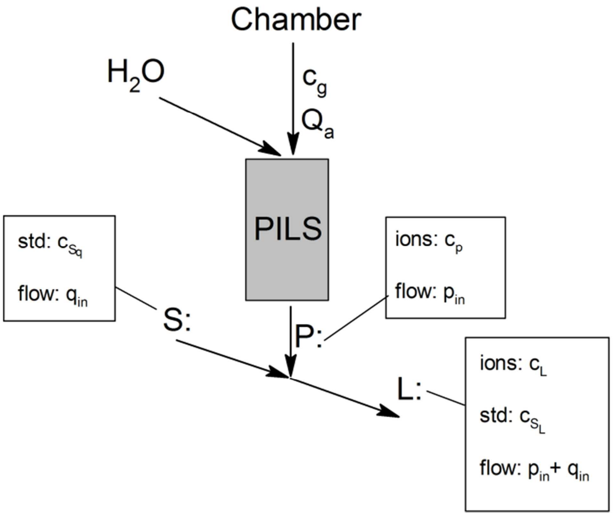

Figure 3.7: Schematic of ingoing and outgoing flows into the PILS and its impactor. S is the flow from the internal standard solution (std), P is the flow of the water droplets grown in the PILS chamber, while L is the flow inside the sample loop, which will be analysed by the IC-system

General Formula: $c_1V_1 = c_2V_2$

Chamber→PILS: $\boldsymbol{c_g = \frac{c_p p_{in}}{Q_a}}$ (8)

P→L: $$\boldsymbol{c_p \times p_{in} = c_L(q_{in} + p_{in})}$$

$$\therefore \boldsymbol{c_g = \frac{c_L(p_{in}+q_{in})}{Q_a}} \tag{9}$$

S→L: $$\boldsymbol{c_{S_q} q_{in} = c_{S_L}(q_{in} + p_{in})}$$

$$\therefore \boldsymbol{p_{in} = q_{in}\left(\frac{c_{S_q}}{c_{S_L}} - 1\right)} \tag{10}$$

Combine **9** and **10:** $$c_g = \frac{c_L}{Q_a}\left(q_{in} + q_{in}\left(\frac{c_{S_q}}{c_{S_L}} - 1\right)\right) = \frac{c_L}{Q_a} \times \frac{c_{S_q}}{c_{S_L}} \times q_{in}$$

With $\boldsymbol{\frac{c_{S_q}}{c_{S_L}} = R}$: $$\boldsymbol{c_g = \frac{c_L q_{in} R}{Q_a}} \tag{11}$$

c_g is the aerosol concentration in the chamber (μg m^{-3}), c_L is the ion concentration detected by the IC-system (μg L^{-1}), q_{in} is the flow of the internal standard at the top of the impactor (L min^{-1}), R is the ratio between the impactor entering and exiting spiked species concentrations (Li^+ for cations, Br^- for anions) and Q_a is the is the flow rate of the air entering the PILS (m^3 min^{-1}). Therefore it is necessary to determine the ingoing (undiluted) concentration of the internal standard (c_{S_q}) (**Section 3.5.1**) and its flow rate into the PILS (q_{in}) (**Section 3.5.2**) in order to gather quantitative data from the PILS-IC.

3.5.1 Make-up

An important aspect of the internal standard is finding a solution, which contains a cation and anion species, which are neither products from particle experiments, nor present in detectable amounts in the atmosphere. For this project procedures from previous publications were followed by using a lithium bromide spiking solution [72].

Two different batches of internal standard were prepared for the MEA experiments (**Chapter 4**). The first was prepared from spectroscopy grade $LiCO_3$ (unknown) and the bromide standard (Fluka), while the second batch was made from lithium bromide (Sigma). **Table 3.10** and **Table 3.11** summarise the solution preparations.

Table 3.10: Preparation of the first internal standard batch. Solution 1.3 was a ~1 L solution, which was used as the spiking solution in the PILS set-up.

Solution	$LiCO_3$[a] / g	H_2O / g	Tot Mass / g	m:m / $g_{solute}/g_{solvent}$	Li^+ conc.	
1.1	0.0138	4.0267	4.0405	0.00343	0.354	g kg^{-1}
1.2	0.0898	3.9216	4.0114	0.0229	0.00811	g kg^{-1}
1.3	1.01	1002.2[b]	1003.21[b]	0.00101	8.17	µg L^{-1}

[a] Solution 1.1 was made from the pure compound, solutions 1.2 and 1.3 were made from the preceding dilution.

[b] This mass also contained 0.2 mL of the 1000 mg L^{-1} bromide stock solution to introduce 200 µg L^{-1} Br^-.

Table 3.11: Preparation of the second internal standard batch. Solution 3.3 was a ~1 L solution, which was used as the spiking solution in the PILS set-up. Solution 3.4 was used as second check for the concentrations.

Solution	LiBr[a] / g	H_2O / g	Tot Mass / g	m:m / $g_{solute}/g_{solvent}$	Li^+ conc.		Br^- conc.	
3.1	0.015	4.0192	4.0342	0.0037	0.30	g kg^{-1}	3.4	g kg^{-1}
3.2	0.0113	4.0003	4.0116	0.00283	0.00084	g kg^{-1}	0.010	g kg^{-1}
3.3	0.296	1079.714	1080.01	0.000274	81	µg L^{-1}	930	µg L^{-1}
	Sol 3.1 / µL	H_2O / µL	Tot Vol / µL	V:V / $V_{solute}/V_{solvent}$	Li^+ conc. / µg L^{-1}		Br^- conc. / µg L^{-1}	
3.4	2383	7617	10000	0.3129	200		2300	

[a] Solution 3.1 was made from the pure compound, solutions 3.2 and 3.3 were made from the preceding dilutions.

Solutions 1.3, 3.3 and 3.4 were injected directly into the IC-system (bypassing the PILS), in order to determine whether the goal concentrations had been achieved. Additionally, the determined concentration would yield the value for c_{S_q}. The results are outlined in **Table 3.12**.

Table 3.12: Results from direct injections of internal standard solutions

Solution	Calc. Li^+ conc. / µg L^{-1}	Detected Li^+ conc. / µg L^{-1}	Discrepancy / %	Calc. Br^- conc. / µg L^{-1}	Detected Br^- conc. / µg L^{-1}	Discrepancy / %
1.3	8.17	8.432	+3.2	—		
3.3	81	69.01	-15.3	937.9	953.2	+1.6
3.4	200	185.3	-7.4	—		

These results show that the readings from the IC-analysis can fluctuate significantly. Due to time constraints, only single injections were performed for each solution. For the next internal standard batch, it is recommended to perform triplicate injections, in order to achieve a higher confidence level for the concentration reading and to examine whether these fluctuations are normal. For the final MEA/NO_x experiment, calculating mixing ratios inside the chamber from the PILS data were achieved by defining c_{S_q} as 69.01 µg L^{-1}.

3.5.2 Flow rate into PILS

The final parameter required for the calculation of the mixing ratios inside the chamber was the flow rate of the internal standard onto the impactor plate. The flow was quantified by measuring the time required to fill a 5 mL volumetric flask. **Table 3.13** summarises the results.

Table 3.13: Results for internal standard flow rate measurements

Run	Time to fill / min	Flow rate / mL min^{-1}
1	12.12	0.4127
2	11.95	0.4184
3	11.95	0.4184
Average	12.01	0.4165
Uncertainty (95%)	0.24	0.0082

From these results q_{in} was defined as 0.4164 ± 0.0082 mL min^{-1}.

3.6 MEA limit of detection (LOD)

As a final preparation for the final MEA/NO_x experiment, it was attempted to find a MEA concentration which would no longer be detected by the IC-system, which could be used for a very rough estimate for the limit of detection (LOD). For this, further dilutions from the MEA stock solution (**Section 3.3.1.3**) were prepared and analysed as shown in **Table 3.14**.

Table 3.14: results from MEA LOD experiments

Solution	Calc. Conc. / µg L^{-1}	Area / µS min cm^{-1}	Measured Conc. / µg L^{-1}	Expected Chamber conc.$^{a, b}$ / µg m^{-3}	Measured Chamber conc.$^{a, c}$ / µg m^{-3}
0.6	0.6385	0.004	1.3	0.017	0.036
0.3	0.3192	0.003	0.9	0.009	0.024
0.15	0.1596	0.006	2.2	0.004	0.059
0.06	0.1064	N/A	N/A	0.003	N/A

[a]Estimated from **Equation 11** (**Section 3.5**) using an average value for c_{S_q} collected from experimental data.

[b]based on the measured area and subsequent extrapolation. [c]based on the calculated concentration

As the MEA concentration in Solution 0.3 was more than sixfold below the previously lowest injected concentration (2 µg L^{-1}), it was analysed first expecting a null result. Unfortunately the analysis of Solution 0.3 proved to be non-quantifiable due to an unstable baseline. Next Solution 0.6 was analysed, yielding higher readings than expected. As a consequence Solution 0.15 was prepared in the anticipation to find the cut-off point. Strangely, Solution 0.15 yielded higher readings than for Solution 0.6. It was assumed that the sample line probably still contained MEA from the previous injections. As a result, after flushing the column and sample lines Solution 0.06 and Solution 0.3 were (re-)assessed. As anticipated, no MEA was detected when analysing Solution 0.06, however, instead of observing a signal drop by a rough factor of two from Solution 0.6 to Solution 0.3, the signal was only 25 % lower. Due to the high discrepancy between the estimates of the expected and measured chamber concentrations, it must be concluded that the concentrations of the analysed standards lie below the limit of quantification (LOQ) and are subjected to baseline interference.

Orsini *et al.* have calculated a LOD of 50 ng m^{-3} for cations and 10 ng m^{-3} for anions [73], while Timonen *et al.* have published a value of 0.1 µg m^{-3} as their LOQ for aerosol sampling [74]. Therefore, when moving forward in this project, a more vigorous analysis is required to be able to precisely determine the LOD and subsequently the LOQ for the IC-system. It is recommended to analyse a 1.8 µg L^{-1} solution in multiple injections, as this concentration corresponds to the published detection limit by Orsini *et al*. The multiple injections is required for the determination of standard deviation, which thereon can be used with the slope from the calibration data in **Equation 12** to obtain proper LOD and LOQ.

$$\boldsymbol{LOD} = \frac{\mathbf{3} \times \boldsymbol{\sigma}}{\boldsymbol{slope_{MEA}}} \quad \text{and} \quad \boldsymbol{LOQ} = \frac{\mathbf{10} \times \boldsymbol{\sigma}}{\boldsymbol{slope_{MEA}}} \tag{12}$$

Chapter 4. MEA chamber experiments

4.1 MEA test injections

Before the first MEA photooxidation experiment was conducted, some test injections were performed to examine whether splitting the manifold did lead to reduced or no particle formation upon MEA injection. Experience gained with the previous chamber suggested that amines could react with residual NO_x in the lines, causing particle formation prior to irradiation [16]. Additionally, it was tested whether the FTIR and PILS-IC could detect MEA.

After it had been established that no particles were formed when injecting MEA with the new sample injection system (**Section 2.3**) and that the FTIR could detect MEA, it was decided to integrate the PILS-IC to the chamber. Unfortunately due to poor alignment, the FTIR was unable to quantify any species *in situ*. The first test experiment was conducted without denuders upstream of the PILS, to later confirm the importance of removing gas-phase species from the sampling stream.

For this experiment, the PILS-IC was set to sample cations and anions every 25 min and Solution 1.3 (**Section 3.5.1**) was used as the internal standard. Simultaneously, clean air was introduced at a rate of 16.5 L min^{-1} into the chamber to counteract the high sampling rate of the PILS. Next MEA (22.3 mg, 0.000365 mol, 357 ppbv) was injected at 53 °C and 2 L min^{-1} for 8 minutes before increasing the injection flow rate to 5 L min^{-1}. At the time of the injection, the humidity was 8.8 %, the temperature was 22.1 °C inside the chamber, while the pressure inside the lab was 1020 mbar. MEA was injected for one hour.

Within 20 minutes of injecting MEA, the PILS-IC successfully started to detect MEA. The readings from the PILS-IC continued to rise throughout the first hour, until a maximum value corresponding to approximate 115 ppbv in the chamber was registered, as shown in **Figure 4.1**. The subsequent slow decline is most likely due to the slow dilution from the zero air make-up counteracting the high gas sampling rate. After 2 hours and 20 minutes the chamber flushing procedure was initiated, which was also observed by the PILS. As throughout the experiment no significant amount of particulate matter was detected by the SMPS-CPC (maximum count: 20 particles cm^{-3}), it was concluded that any MEA detected by the PILS-IC system had to be from the gas-phase.

During the experiment, the PILS-IC also detected minor contaminants, such as NH_4^+, Na^+, F^-, Acetate, Cl^-, NO_2^-, NO_3^- and PO_4^{3-}. These contaminants came from three possible sources: first in very small quantities from within the chamber, secondly ambient inorganics, such as sulfates, chloride and ammonia could have slowly dissolved from the atmosphere into the ultrapure water stored in bottles and thirdly the internal standard, which was probably the highest contributor of contaminants due to sample preparation.

Assuming complete transfer of the MEA from the injection vessel into the chamber, the mixing ratio for MEA should be 357 ppbv. However, the highest reading from the PILS only correlated to a mixing ratio of ~115 ppbv, which is only 32 % of the assumed chamber concentration. This low reading could be due to factors such as incomplete transfer into the chamber or poor efficiency of dissolving gas-phase molecules into the high-purity water in the PILS. The latter is the more likely explanation, as the PILS was developed to dissolve water-soluble particulate matter and not gas-phase molecules. Therefore comparing this experiment and the subsequent particle generation experiment should indicate the validity of this hypothesis.

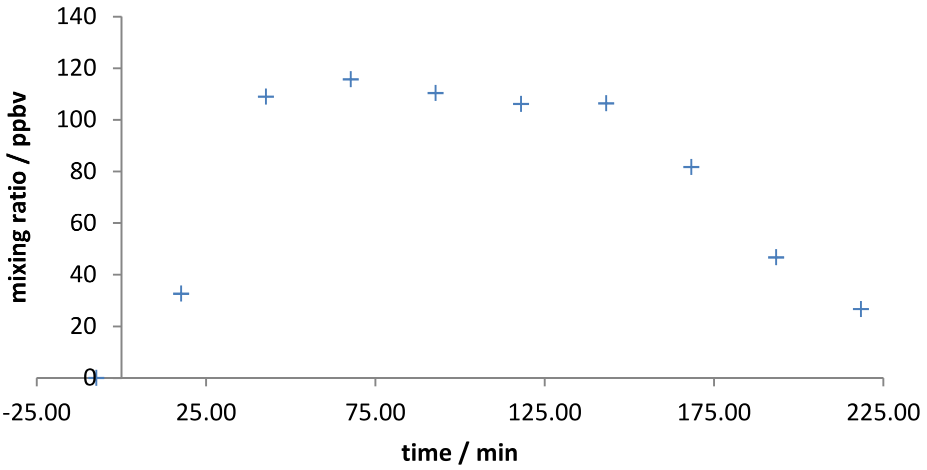

Figure 4.1: Chamber concentrations calculated based on Equation 9 (Section 3.4). Maximum reading corresponded to ~115 ppbv MEA in the chamber, which is only 32 % of the injected 357 ppbv. The decline after 143 min is due to the flushing of the chamber, which replaces chamber contents with clean air.

4.2 MEA photooxidation experiment

After the successful injection of MEA and its detection by the PILS-IC system, a first MEA particle generation experiment was conducted. Unfortunately the hard disk on the computer running Labview failed the day before the experiment, requiring manual logging of mixing ratios, which lead to a poor time-resolution for the changing atmosphere inside the chamber. Additionally, the internal temperature could not be monitored.

For this experiment, the PILS-IC was set to sample cations and anions every 25 min, Solution 3.3 (**Section 3.5.1**) was used as the internal standard and no denuders were installed upstream of the PILS, as their coating was not finished on time. After sealing the chamber, determining the internal RH (8.0 %) and temperature (22.6 °C) and allowing the PILS-IC to equilibrate, MEA (24.2 mg, 0.000396 mol, 388 ppbv) was injected for an hour, where the line was initially heated to 58 °C but rose to 65 °C during the hour. Due to maintenance, the zero air plant had to be shut down. As a consequence, no air pulses could be introduced to enhance the mixing. Therefore the injected MEA was left to mix through diffusion for an hour before continuing the experiment. As illustrated in **Figure 4.2**, no significant changes to the gas mixing ratios could be observed during this time period. During the injection period, it was discovered that the PILS was not providing the IC with a continuous flow of aerosol-water. Therefore the automatic sampling had to be deactivated and it was attempted to fix the flow problem. Eventually it was apparent that IC-analysis of the aerosol water was only sporadically possible. As a consequence, readings were only taken when it was certain that the sample loop was neither dry, nor contained large air bubbles, which could destroy the column coating upon analysis.

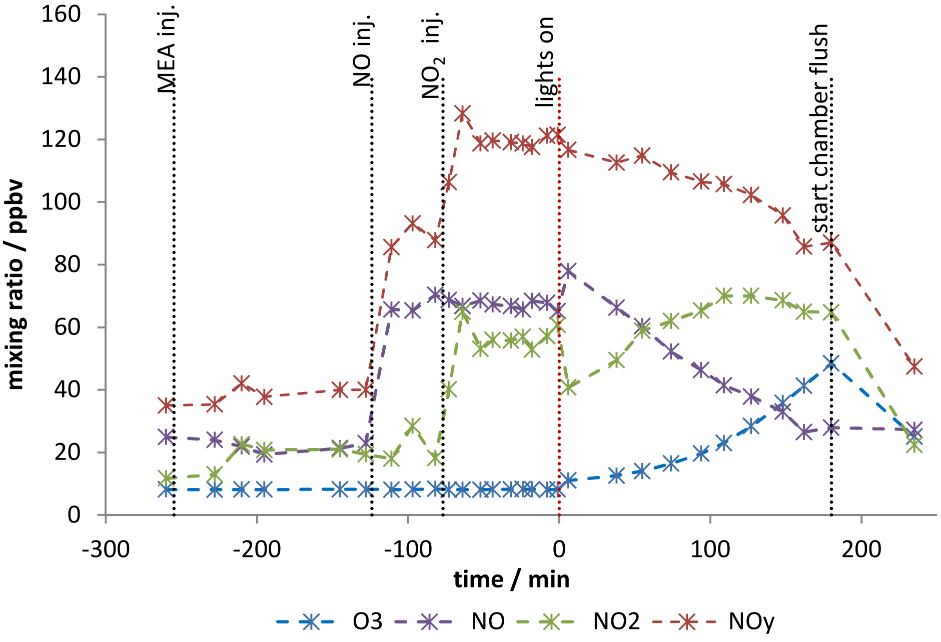

Figure 4.2: Profile of prominent gases inside the chamber. Data had to be recorded manually due to data logger failure. The points of injections and the start of flushing the chamber are marked in black dotted lines, while the moment the UV-lights are switched on is marked in a red dotted line, which equates to time Zero.

Next, 30 ± 1 ppbv NO was injected and allowed to equilibrate. The introduction of NO was registered by the monitoring devices, as shown in **Figure 4.2** above. The SMPS-CPC did not detect any particles, while the PILS-IC indicated no change to MEA concentration. After the equilibration period, 58 ± 1 ppbv NO_2 was injected, which surprisingly lead to particle generation (see **Figure xI.4** in Appendix). These particles are potentially the result of an acid-base reaction between MEA and HNO_3, a product of water vapour and NO_2. Additional to observed particles, the assumption that the PILS is not efficient in dissolving gaseous molecules into ultrapure water was tentatively confirmed. Prior to the injection the PILS-IC was reading chamber mixing ratios of 110-140 ppbv (27-36 %), but after the NO_2 injection a MEA mixing ratio of 294 ppbv was detected. This corresponds to 75 % of the assumed injected concentration. Therefore NO_2 somehow activated MEA or made it more accessible to dissolution. Additionally, based on **Figure 4.4**, it is also possible that some MEA degradation or transformation is occurring during the acid-base reactions, as a slight increase in nitrate and acetate concentrations was observed. Unfortunately, only one data point was collected after the injection of NO_2. As a consequence, the activation or transformation cannot be confirmed.

Several observations were made after the UV-light were turned on. First, the particle volume starts to increase throughout the three hours prior to flushing (see **Figure xI.4** in Appendix). Simultaneously, a decline in MEA concentrations and a significant increase in ammonium and acetate levels were detected by the PILS-IC (see **Figures 4.3** and **4.4**). This is expected, as they are both products of MEA photooxidation. Additionally, during the three hours of irradiation, ozone levels rose to ~48.5 ppbv, NO declined to ~87.0 ppbv, while NO_2 rose to ~64.8 ppbv. These are all indicators for the photooxidative process, where VOCs consume NO to yield NO_2 and disrupt the cycle that breaks down O_3 to O_2 and molecular oxygen.

As the PILS data was collected without the use of denuders, it cannot be differentiated whether the observed increase in nitrate, acetate and ammonium concentrations are a consequence of either increasing levels of these species in gas form, or whether they increasingly contribute to the particulate mass. Furthermore, due to the poor time resolution of the collected data, only trends are observable. Therefore no clear statements are possible on the significance of the increasing or decreasing levels of the targeted species.

For future experiments, one should not only consider attaching the denuders to the fully functioning PILS, which should yield a better understanding of particulate matter composition, but also performing the same experiments with longer IC-run times to detect possible products from particle-phase reactions that yield long chain oligomers. These would have much higher retention times than the single building blocks, such as acetate, glycolate and oxalate.

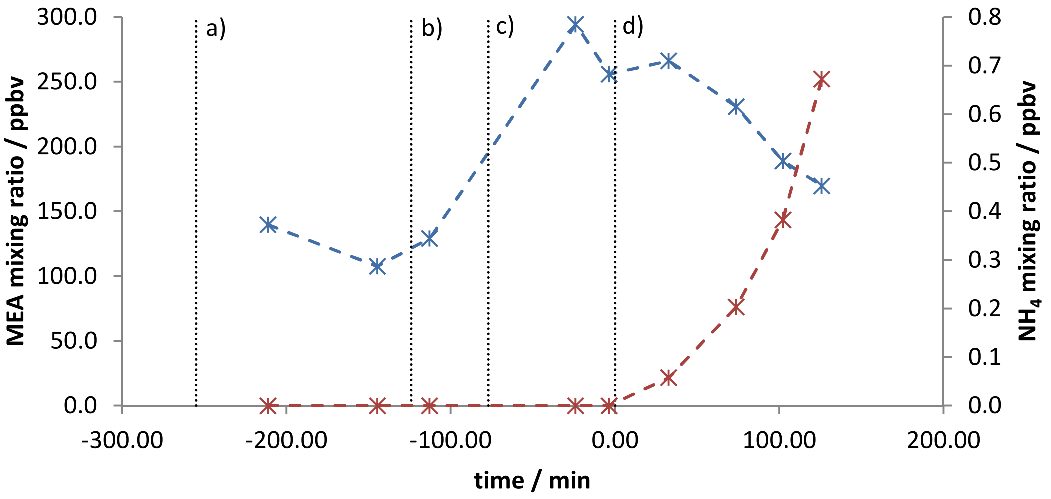

Figure 4.3: MEA (blue) and ammonium (red) concentrations in chamber according to PILS-IC readings. Point a) marks the injection of MEA, point b) is the injection of NO, point c) is the injection of NO_2 and lastly point d) is when the UV-lights were turned on.

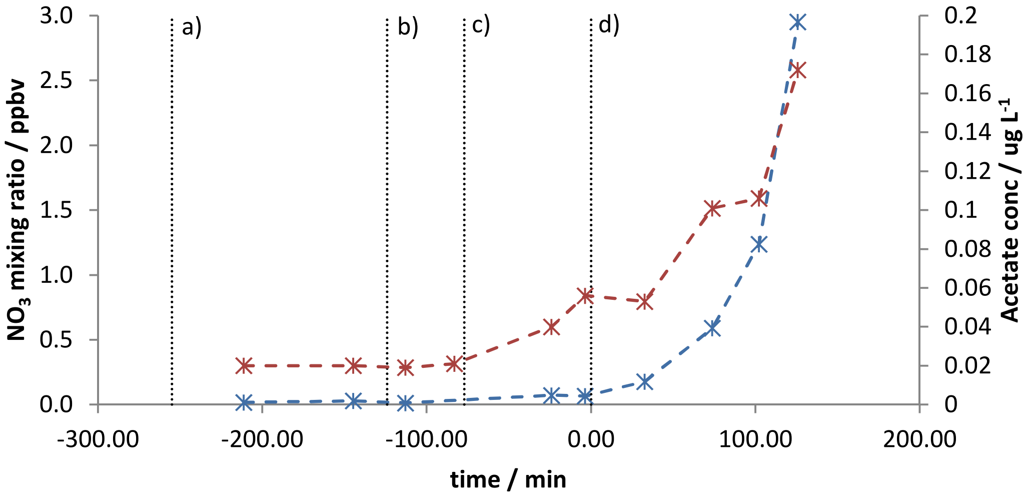

Figure 4.4: Nitrate (blue) concentration in chamber according to PILS-IC readings and Acetate (red) concentrations detected in aerosol-water. Point a) marks the injection of MEA, point b) is the injection of NO, point c) is the injection of NO_2 and lastly point d) is when the UV-lights were turned on. The IC-system is not calibrated for acetate at this stage. Therefore no conversion into ppbv was possible.

Chapter 5. Conclusions and Outlook

This project aims to investigate the nucleation behaviour of amines released into the atmosphere by CCS technology. Yet, before nucleation-specific experiments could be conducted, CSIRO's new third generation environmental chamber was commissioned and fitted with analytical instruments tuned for the analysis of amine-based aerosol. The integration of the PILS-IC to the chamber required several experiments to determine a selection of properties and auxiliary reactions, the results of which are presented in this work. These include the development of a procedure for removing contaminants and remnants from previous experiments by a standardised NO_x/propene experiment, the determination of the NO_2 photolysis rate (0.512 ± 0.027 s^{-1}), the wall loss rate of ozone $(5.6112 \pm 0.0011) \times 10^{-7}$ s^{-1} and the wall loss coefficient β for particles in the bins 54.1 – 181.1 nm. However, there are still several auxiliary mechanisms which require attention, such as the HONO production from the Teflon walls, the hydrolysis of NO_2 and N_2O_5, and the wall loss rates for NO, NO_2, propene and HNO_3.

Additionally to the auxiliary mechanisms, some of the analytical devices require refinements, such as the installation of a dehumidifier for the zero air plant, the alignment of the long-path FTIR to obtain quantifiable data and the installation of the denuders for the PILS-IC. Furthermore, for future experiments the PILS requires regular and vigorous cleaning. After the final experiment the disassembly of the device lead to the discovery that the failure to provide a continuous stream of aerosol-water was probably due to a build-up of residual particulate matter in the sample drain.

Nevertheless, despite the poor time resolution, the final experiment was successful in showing some expected trends, such as the decrease of MEA and the increase of organic ions, such as ammonium, acetate and nitrate, the moment the UV lights were turned on. Yet, as no denuders were used, these preliminary data do not allow for any interpretation on the composition of the generated aerosol during the irradiation experiment. Therefore, the final experiment has to be repeated with installed denuders. Furthermore, the scope of the project should be broadened to other amine systems to test the robustness and versatility of the developed methodology during this project.

In summary, while the primary aim of investigating the amine-aerosol nucleation process(es) was not achieved, good progress was made in setting up a method by which this will be accomplished in the next stage.

References

1. Seinfeld, J.H. and S.N. Pandis, *Atmospheric chemistry and physics: from air pollution to climate change*1998: Wiley.
2. Jacobson, M.Z., *Fundamentals of Atmospheric Modeling*2005: Cambridge University Press.
3. Pöschl, U., *Atmospheric Aerosols: Composition, Transformation, Climate and Health Effects.* Angew. Chem. Int. Ed., 2005. 44(46): p. 7520-7540.
4. Cohen, A.J., et al., *The Global Burden of Disease Due to Outdoor Air Pollution.* J. Toxicol. Environ. Health, Part A, 2005. 68(13-14): p. 1301-1307.
5. Bellouin, N., et al., *Estimates of aerosol radiative forcing from the MACC re-analysis.* Atmos. Chem. Phys., 2013. 13(4): p. 2045-2062.
6. IPCC, *Climate Change 2013: The Physical Science Basis. Contribution of Working Group I to the Fifth Assessment Report of the Intergovernmental Panel on Climate Change* 2013, Cambridge, United Kingdom and New York, NY, USA: Cambridge University Press. 1535.
7. Trivitayanurak, W. and P.J. Adams, *Does the POA–SOA split matter for global CCN formation?* Atmos. Chem. Phys., 2014. 14(2): p. 995-1010.
8. Kroll, J.H. and J.H. Seinfeld, *Chemistry of secondary organic aerosol: Formation and evolution of low-volatility organics in the atmosphere.* Atmos. Environ., 2008. 42(16): p. 3593-3624.
9. Fuzzi, S., et al., *Critical assessment of the current state of scientific knowledge, terminology, and research needs concerning the role of organic aerosols in the atmosphere, climate, and global change.* Atmos. Chem. Phys., 2006. 6(7): p. 2017-2038.
10. Kulmala, M., *How Particles Nucleate and Grow.* Science, 2003. 302(5647): p. 1000-1001.
11. Kulmala, M., et al., *Initial steps of aerosol growth.* Atmos. Chem. Phys., 2004. 4(11/12): p. 2553-2560.
12. Murphy, S.M., et al., *Secondary aerosol formation from atmospheric reactions of aliphatic amines.* Atmos. Chem. Phys., 2007. 7(9): p. 2313-2337.
13. Veltman, K., B. Singh, and E.G. Hertwich, *Human and Environmental Impact Assessment of Postcombustion CO2 Capture Focusing on Emissions from Amine-Based Scrubbing Solvents to Air.* Environ. Sci. Technol., 2010. 44(4): p. 1496-1502.
14. Bzdek, B.R., D.P. Ridge, and M.V. Johnston, *Amine exchange into ammonium bisulfate and ammonium nitrate nuclei.* Atmos. Chem. Phys., 2010. 10(8): p. 3495-3503.
15. Zhao, J., et al., *Observation of neutral sulfuric acid-amine containing clusters in laboratory and ambient measurements.* Atmos. Chem. Phys., 2011. 11(21): p. 10823-10836.
16. Angove, D., et al., *Deliverable 4.2: Determination of the fate of PCC emissions into the atmosphere*, 2013, ABLEC R&D. CSIRO, Australia.
17. Goldstein, A.H. and I.E. Galbally, *Known and Unexplored Organic Constituents in the Earth's Atmosphere.* Environ. Sci. Technol., 2007: p. 1515-1521.
18. Hallquist, M., et al., *The formation, properties and impact of secondary organic aerosol: current and emerging issues.* Atmos. Chem. Phys., 2009. 9(14): p. 5155-5236.
19. Bellouin, N.O.J.M.S., *Global estimate of aerosol direct radiative forcing from satellite measurements.* Nature, 2005. 438(7071): p. 1138-1141.
20. Sorooshian, A., et al., *On the link between ocean biota emissions, aerosol, and maritime clouds: Airborne, ground, and satellite measurements off the coast of California.* Glob. Biogeochem. Cy., 2009. 23(4): p. GB4007.
21. Jang, M., et al., *Heterogeneous Atmospheric Aerosol Production by Acid-Catalyzed Particle-Phase Reactions.* Science, 2002. 298(5594): p. 814-817.
22. Nemmar, A., et al., *Passage of inhaled particles into the blood circulation in humans.* Circulation, 2002. 105(4): p. 411-4.
23. Oberdörster, G., et al., *Translocation of Inhaled Ultrafine Particles to the Brain.* Inhal. Toxicol., 2004. 16(6-7): p. 437-445.

24. O'Dowd, C.D., et al., *Biogenically driven organic contribution to marine aerosol.* Nature, 2004. 431(7009): p. 676-680.
25. Chow, J.C., et al., *The IMPROVE_A Temperature Protocol for Thermal/Optical Carbon Analysis: Maintaining Consistency with a Long-Term Database.* J. Air Waste Manage., 2007. 57(9): p. 1014-1023.
26. Atkinson, R. and J. Arey, *Gas-phase tropospheric chemistry of biogenic volatile organic compounds: a review.* Atmos. Environ., 2003. 37, Supplement 2(0): p. 197-219.
27. Kesselmeier, J. and M. Staudt, *Biogenic Volatile Organic Compounds (VOC): An Overview on Emission, Physiology and Ecology.* J. Atmos. Chem., 1999. 33(1): p. 23-88.
28. Cheng, Y. and S.-M. Li, *Analytical method development of long-chain ketones in PM2.5 aerosols using accelerated solvent extraction and Gc/FID/MSD.* Int. J. Environ. An. Ch., 2004. 84(5): p. 367-378.
29. Baltrėnas, P., et al., *Atmospheric BTEX concentrations in the vicinity of the crude oil refinery of the Baltic region.* Environ. Monit. Assess., 2011. 182(1-4): p. 115-127.
30. Lee, S.C., et al., *Volatile organic compounds (VOCs) in urban atmosphere of Hong Kong.* Chemosphere, 2002. 48(3): p. 375-382.
31. Talapatra, A. and A. Srivastava, *Ambient Air Non-Methane Volatile Organic Compound (NMVOC) Study Initiatives in India–A Review.* Journal of Environmental Protection, 2011. 2(1): p. 21-36.
32. Kanakidou, M., et al., *Organic aerosol and global climate modelling: a review.* Atmos. Chem. Phys., 2005. 5(4): p. 1053-1123.
33. Kulmala, M., L. Pirjola, and J.M. Makela, *Stable sulphate clusters as a source of new atmospheric particles.* Nature, 2000. 404(6773): p. 66-69.
34. O'Dowd, C.D., et al., *Marine aerosol formation from biogenic iodine emissions.* Nature, 2002. 417(6889): p. 632-636.
35. Rabaud, N.E., et al., *Characterization and quantification of odorous and non-odorous volatile organic compounds near a commercial dairy in California.* Atmos. Environ., 2003. 37(7): p. 933-940.
36. Facchini, M.C., et al., *Important Source of Marine Secondary Organic Aerosol from Biogenic Amines.* Environ. Sci.Technol., 2008. 42(24): p. 9116-9121.
37. Cornell, S.E., et al., *Organic nitrogen deposition on land and coastal environments: a review of methods and data.* Atmos. Environ., 2003. 37(16): p. 2173-2191.
38. Almeida, J., et al., *Molecular understanding of sulphuric acid-amine particle nucleation in the atmosphere.* Nature, 2013. 502(7471): p. 359-363.
39. Barnes, I., et al., *Aspects of the Atmospheric Chemistry of Amides.* ChemPhysChem, 2010. 11(18): p. 3844-3857.
40. DuPart, M.S., P.C. Rooney, and T.R. Bacon, *Comparing laboratory and plant data for MDEA/DEA blends.* Hydrocarbon Process., 1999. 78(4): p. 81.
41. Rooney, P.C., M.S. DuPart, and T.R. Bacon, *Oxygen's role in alkanolamine degradation.* Hydrocarbon Process., 1998. 77(7): p. 109.
42. Kurtén, T., et al., *Amines are likely to enhance neutral and ion-induced sulfuric acid-water nucleation in the atmosphere more effectively than ammonia.* Atmos. Chem. Phys., 2008. 8(14): p. 4095-4103.
43. Petäjä, T., et al., *Experimental Observation of Strongly Bound Dimers of Sulfuric Acid: Application to Nucleation in the Atmosphere.* Phys. Rev. Lett., 2011. 106(22): p. 228302.
44. Pitts, J.N., et al., *Photooxidation of aliphatic amines under simulated atmospheric conditions: formation of nitrosamines, nitramines, amides, and photochemical oxidant.* Environ. Sci. Technol., 1978. 12(8): p. 946-953.
45. Nemmar, A., et al., *Ultrafine Particles Affect Experimental Thrombosis in an In Vivo Hamster Model.* Am. J.Resp. Crit. Care, 2002. 166(7): p. 998-1004.
46. Schade, G. and P. Crutzen, *Emission of aliphatic amines from animal husbandry and their reactions: Potential source of N2O and HCN.* J. Atmos. Chem., 1995. 22(3): p. 319-346.

47. Nielsen, C.J., H. Herrmann, and C. Weller, *Atmospheric chemistry and environmental impact of the use of amines in carbon capture and storage (CCS).* Chem. Soc. Rev., 2012. 41(19): p. 6684-704.
48. Claeys, M., et al., *Formation of Secondary Organic Aerosols Through Photooxidation of Isoprene.* Science, 2004. 303(5661): p. 1173-1176.
49. Fisseha, R., et al., *Determination of primary and secondary sources of organic acids and carbonaceous aerosols using stable carbon isotopes.* Atmos. Environ., 2009. 43(2): p. 431-437.
50. Reisinger, P., et al., *Intercomparison of measurement techniques for black or elemental carbon under urban background conditions in wintertime: influence of biomass combustion.* Environ. Sci. Technol., 2008. 42(3): p. 884-9.
51. Chiappini, L., et al., *Development of a supercritical fluid extraction–gas chromatography–mass spectrometry method for the identification of highly polar compounds in secondary organic aerosols formed from biogenic hydrocarbons in smog chamber experiments.* Anal. Bioanal. Chem., 2006. 386(6): p. 1749-1759.
52. Veltkamp, P.R., et al., *Chromatographic measurement of molecular markers of sources of atmospheric aerosol particles.* Environ. Geochem. Health, 1996. 18(2): p. 77-80.
53. Canagaratna, M.R., et al., *Chemical and microphysical characterization of ambient aerosols with the aerodyne aerosol mass spectrometer.* Mass. Spectrom. Rev., 2007. 26(2): p. 185-222.
54. Jayne, J.T., et al., *Development of an Aerosol Mass Spectrometer for Size and Composition Analysis of Submicron Particles.* Aerosol Sci. Tech., 2000. 33(1-2): p. 49-70.
55. Takegawa, N., et al., *Characterization of an Aerodyne Aerosol Mass Spectrometer (AMS): Intercomparison with Other Aerosol Instruments.* Aerosol Sci. Tech., 2005. 39(8): p. 760-770.
56. Bernstein, J.A., et al., *Health effects of air pollution.* J. Allergy Clin. Immun., 2004. 114(5): p. 1116-1123.
57. Angove, D., et al., *Investigation of the Atmospheric Photochemistry of the CO2 Capture Solvent, Monoethanolamine (MEA) Under Controlled Conditions. Final Report for Norsk Energi and Gassnova*, 2010a, CSIRO
58. Hynes, R.G., et al., *Evaluation of two MCM v3.1 alkene mechanisms using indoor environmental chamber data.* Atmos. Environ., 2005. 39(38): p. 7251-7262.
59. Bloss, C., et al., *Development of a detailed chemical mechanism (MCMv3.1) for the atmospheric oxidation of aromatic hydrocarbons.* Atmos. Chem. Phys., 2005. 5(3): p. 641-664.
60. Carter, W.P.L. and F.W. Lurmann, *Evaluation of a detailed gas-phase atmospheric reaction mechanism using environmental chamber data.* Atmos. Environ. A-Gen., 1991. 25(12): p. 2771-2806.
61. Edney, E.O., et al., *Impact of aerosol liquid water on secondary organic aerosol yields of irradiated toluene/propylene/NOx/(NH4)2SO4/air mixtures.* Atmos. Environ., 2000. 34(23): p. 3907-3919.
62. Jeffries, H., D. Fox, and R. Kamens, *Outdoor smog chamber studies: light effects relative to indoor chambers.* Environ. Sci. Technol., 1976. 10(10): p. 1006-1011.
63. Atkinson, R., et al., *Evaluated kinetic and photochemical data for atmospheric chemistry: Volume I - gas phase reactions of Ox, HOx, NOx and SOx species.* Atmos. Chem. Phys., 2004. 4(6): p. 1461-1738.
64. Wang, X., et al., *Design and characterization of a smog chamber for studying gas-phase chemical mechanisms and aerosol formation.* Atmos. Meas. Tech., 2014. 7(1): p. 301-313.
65. Singh, L., *Wall Loss Correction Determination for Smog Chamber Experiments*, 2008, CSIRO: Lucas Heights.
66. McMurry, P.H. and D.J. Rader, *Aerosol Wall Losses in Electrically Charged Chambers.* Aerosol Sci. Technol., 1985. 4(3): p. 249-268.

67. Crump, J.G. and J.H. Seinfeld, *Turbulent deposition and gravitational sedimentation of an aerosol in a vessel of arbitrary shape.* J. Aerosol Sci., 1981. 12(5): p. 405-415.
68. Fuchs, N.A., *The Mechanics of Aerosols*, ed. C.N. Davies1964, London: Pergamon.
69. Takekawa, H., H. Minoura, and S. Yamazaki, *Temperature dependence of secondary organic aerosol formation by photo-oxidation of hydrocarbons.* Atmos. Environ., 2003. 37(24): p. 3413-3424.
70. Cocker, D.R., 3rd, R.C. Flagan, and J.H. Seinfeld, *State-of-the-art chamber facility for studying atmospheric aerosol chemistry.* Environ. Sci. Technol., 2001. 35(12): p. 2594-601.
71. Rohrer, F., et al., *Characterisation of the photolytic HONO-source in the atmosphere simulation chamber SAPHIR.* Atmos. Chem. Phys., 2005. 5(8): p. 2189-2201.
72. Tang, X., et al., *NO3 radical, OH radical and O3-initiated secondary aerosol formation from aliphatic amines.* Atmos. Environ., 2013. 72(0): p. 105-112.
73. Orsini, D.A., et al., *Refinements to the particle-into-liquid sampler (PILS) for ground and airborne measurements of water soluble aerosol composition.* Atmos. Environ., 2003. 37(9–10): p. 1243-1259.
74. Timonen, H., et al., *High time-resolution chemical characterization of the water-soluble fraction of ambient aerosols with PILS-TOC-IC and AMS.* Atmos. Meas. Tech., 2010. 3(4): p. 1063-1074.

Appendix I

Table xI.1: Particle wall loss rates and their uncertainties

Bin / nm	51.4	53.3	55.2	57.3	59.4	61.5
Rate / min^{-1}	$(6.2 \pm 5.5) \times 10^{-4}$	$(-3.1 \pm 6.8) \times 10^{-4}$	$(1.52 \pm 0.39) \times 10^{-3}$	$(1.36 \pm 0.39) \times 10^{-3}$	$(8.7 \pm 3.1) \times 10^{-4}$	$(1.29 \pm 0.33) \times 10^{-3}$

Bin / nm	63.8	66.1	68.5	71	73.7	76.4
Rate / min^{-1}	$(1.63 \pm 0.24) \times 10^{-3}$	$(1.44 \pm 0.22) \times 10^{-3}$	$(1.30 \pm 0.20) \times 10^{-3}$	$(1.22 \pm 0.17) \times 10^{-3}$	$(1.51 \pm 0.15) \times 10^{-3}$	$(1.24 \pm 0.12) \times 10^{-3}$

Bin / nm	79.1	82	85.1	88.2	91.4	94.7
Rate / min^{-1}	$(1.47 \pm 0.14) \times 10^{-3}$	$(1.11 \pm 0.13) \times 10^{-3}$	$(1.15 \pm 0.13) \times 10^{-3}$	$(1.02 \pm 0.10) \times 10^{-3}$	$(1.115 \pm 0.092) \times 10^{-3}$	$(9.73 \pm 0.85) \times 10^{-4}$

Bin / nm	98.2	101.8	105.5	109.4	113.4	117.6
Rate / min^{-1}	$(1.080 \pm 0.085) \times 10^{-3}$	$(9.54 \pm 0.86) \times 10^{-4}$	$(1.022 \pm 0.079) \times 10^{-3}$	$(7.70 \pm 0.75) \times 10^{-4}$	$(8.18 \pm 0.77) \times 10^{-4}$	$(9.55 \pm 0.80) \times 10^{-4}$

Bin / nm	121.9	126.3	131	135.8	140.7	145.9
Rate / min^{-1}	$(8.04 \pm 0.82) \times 10^{-4}$	$(6.58 \pm 0.80) \times 10^{-4}$	$(6.64 \pm 0.75) \times 10^{-4}$	$(6.61 \pm 0.82) \times 10^{-4}$	$(6.47 \pm 0.78) \times 10^{-4}$	$(4.69 \pm 0.90) \times 10^{-4}$

Bin / nm	151.2	156.8	162.5	168.5	174.7	181.1
Rate / min^{-1}	$(5.45 \pm 0.86) \times 10^{-4}$	$(5.85 \pm 0.81) \times 10^{-4}$	$(2.17 \pm 0.87) \times 10^{-4}$	$(4.0 \pm 1.1) \times 10^{-4}$	$(2.3 \pm 1.0) \times 10^{-4}$	$(3.2 \pm 1.2) \times 10^{-4}$

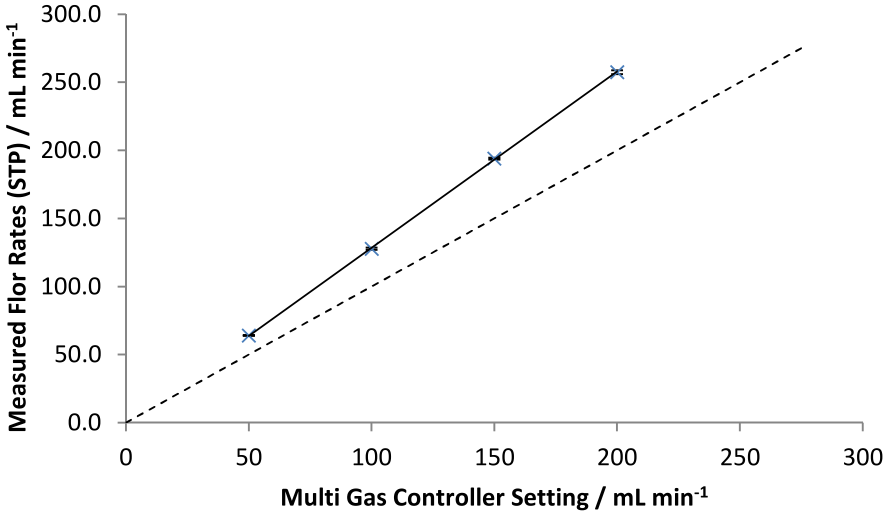

Figure xI.1: Calibration plot for Mass Flow Controller 2l, which is used to inject NO2/He. Regression statistics yielded a slope of 1.2930 ± 0.0075, an intercept of -0.9 ± 1.0 mL min^{-1}, R^{2} of 0.9999 and a residual sum of squares of 1.423 mL^{2} min^{-2}.

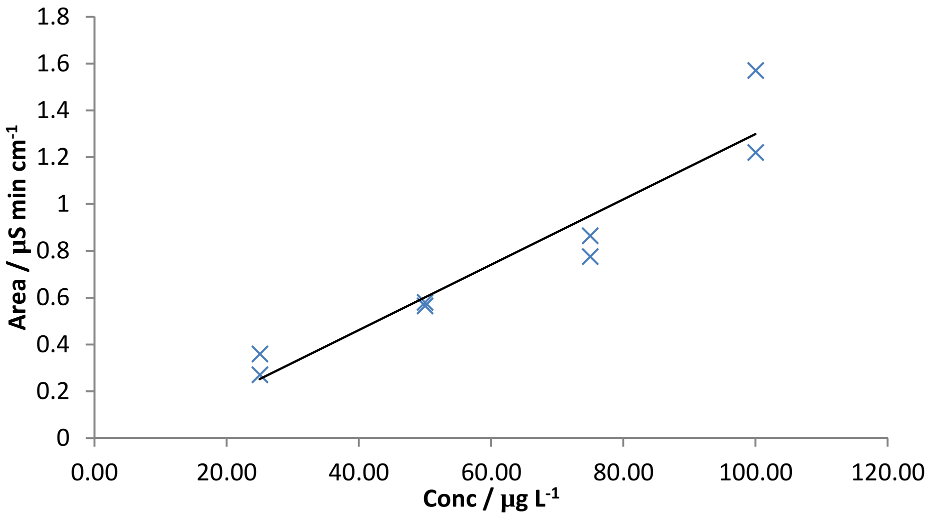

Figure xI.2: Calibration plot for sodium. Regression statistics yield a slope of 0.0140 ± 0.0019 µS min L cm^{-1} µg^{-1}, an intercept of -0.10 ± 0.13 µS min cm^{-1}, R^{2} of 0.9023 and a residual sum of squares of 0.1318 µS^{2} min^{2} cm^{-2}. The highest reading for 100 µg L^{-1} is a suspected outlier.

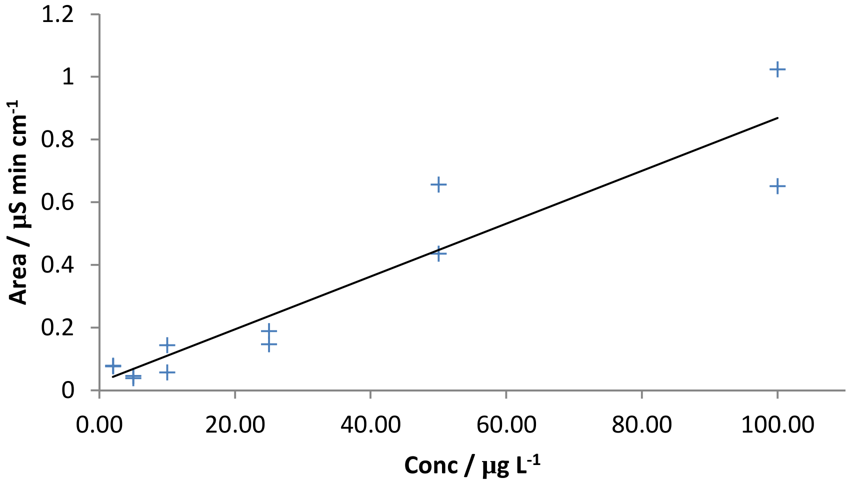

Figure xI.3: Measured sodium contaminations for the corresponding MEA dilutions. Due to the rising trend, it was assumed that the contaminants were introduced in the first step of sample preparation

Table xI.2: Grubbs test for the two suspected outliers for bromine calibration

Dilution Series	Concentration	Value	Mean	SD	Grubbs crit. Value	Q	Outlier?
1	75 µg L^{-1}	0.103	0.0977	0.0039	1.15	1.38	Yes
1	100 µg L^{-1}	0.117	0.125	0.0059	1.15	1.39	Yes

Table xI.3: Grubbs test for the two suspected outliers for nitrate calibration

Dilution Series	Concentration	Value	Mean	SD	Grubbs crit. Value	Q	Outlier?
1	10 µg L^{-1}	0.038	0.022	0.012	1.15	1.36	Yes
2	100 µg L^{-1}	0.234	0.204	0.021	1.15	1.40	Yes

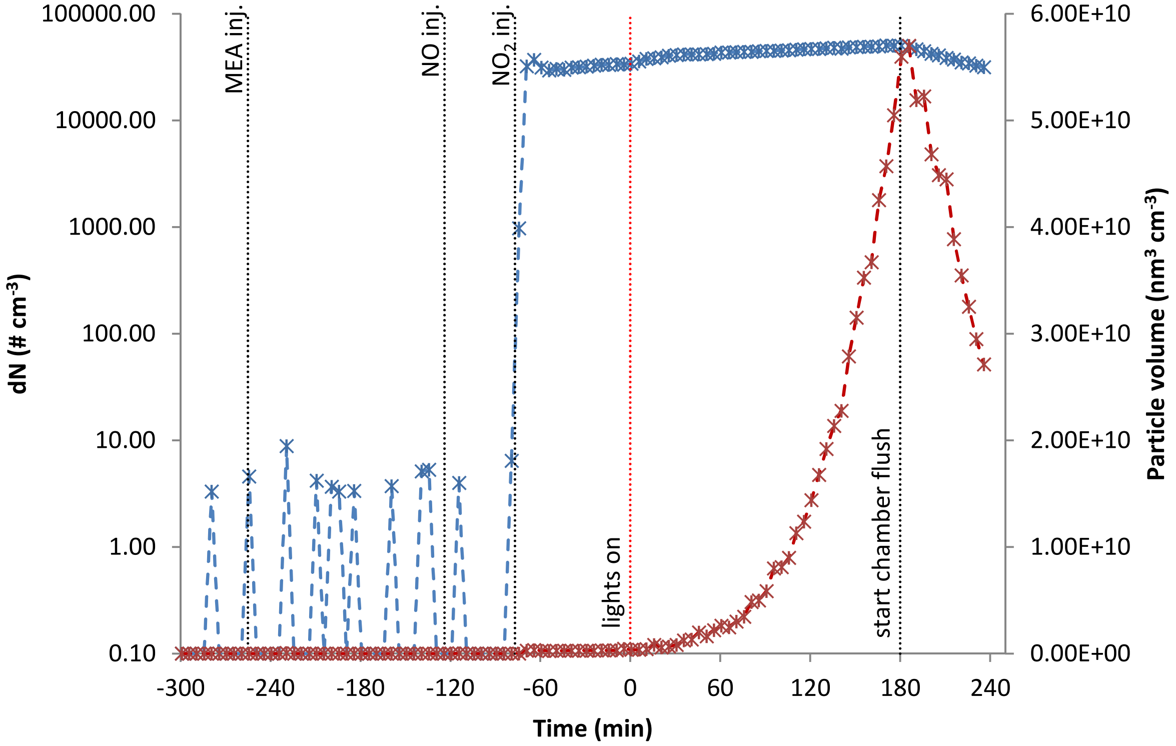

Figure xI.4: Corrected particle number (blue) and volume (red) for the MEA photooxidation experiment (Section 4.2).